J. Fluid Mech. (2010), *vol.* 662, *pp.* 409–446.
doi:10.1017/S0022112010003290

Numerical simulations of Rayleigh–Bénard convection for Prandtl numbers between 10^{-1} and 10^4 and Rayleigh numbers between 10^5 and 10^9

G. SILANO[1,2], K. R. SREENIVASAN[2,3] AND R. VERZICCO[4,5]†

[1]Università degli Studi di Trieste, DMI, 34127 Trieste, Italy

[2]International Centre for Theoretical Physics, 34014 Trieste, Italy

[3]Courant Institute of Mathematical Sciences and Department of Physics, New York University, NY 10012, USA

[4]Università di Roma 'Tor Vergata', DIM, 00133 Rome, Italy

[5]University of Twente, PoF, 7500 AE, Enschede, The Netherlands

(Received 9 October 2009; revised 14 June 2010; accepted 15 June 2010; first published online 14 September 2010)

We summarize the results of an extensive campaign of direct numerical simulations of Rayleigh–Bénard convection at moderate and high Prandtl numbers ($10^{-1} \leqslant Pr \leqslant 10^4$) and moderate Rayleigh numbers ($10^5 \leqslant Ra \leqslant 10^9$). The computational domain is a cylindrical cell of aspect ratio $\Gamma = 1/2$, with the no-slip condition imposed on all boundaries. By scaling the numerical results, we find that the free-fall velocity should be multiplied by $1/\sqrt{Pr}$ in order to obtain a more appropriate representation of the large-scale velocity at high Pr. We investigate the Nusselt and the Reynolds number dependences on Ra and Pr, comparing the outcome with previous numerical and experimental results. Depending on Pr, we obtain different power laws of the Nusselt number with respect to Ra, ranging from $Ra^{2/7}$ for $Pr = 1$ up to $Ra^{0.31}$ for $Pr = 10^3$. The Nusselt number is independent of Pr. The Reynolds number scales as $Re \sim \sqrt{Ra}/Pr$, neglecting logarithmic corrections. We analyse the global and local features of viscous and thermal boundary layers and their scaling behaviours with respect to Ra and Pr, and with respect to the Reynolds and Péclet numbers. We find that the flow approaches a saturation state when Reynolds number decreases below the critical value, $Re_s \simeq 40$. The thermal-boundary-layer thickness increases slightly (instead of decreasing) when the Péclet number increases, because of the moderating influence of the viscous boundary layer. The simulated ranges of Ra and Pr contain steady, periodic and turbulent solutions. A rough estimate of the transition from the steady to the unsteady state is obtained by monitoring the time evolution of the system until it reaches stationary solutions. We find multiple solutions as long-term phenomena at $Ra = 10^8$ and $Pr = 10^3$, which, however, do not result in significantly different Nusselt numbers. One of these multiple solutions, even if stable over a long time interval, shows a break in the mid-plane symmetry of the temperature profile. We analyse the flow structures through the transitional phases by direct visualizations of the temperature and velocity fields. A wide variety of large-scale circulation and plume structures has been found. The single-roll circulation is

† Email address for correspondence: verzicco@uniroma2.it

characteristic only of the steady and periodic solutions. For other regimes at lower Pr, the mean flow generally consists of two opposite toroidal structures; at higher Pr, the flow is organized in the form of multi-jet structures, extending mostly in the vertical direction. At high Pr, plumes mainly detach from sheet-like structures. The signatures of different large-scale structures are generally well reflected in the data trends with respect to Ra, less in those with respect to Pr.

Key words: Turbulent convection, boundary layer structure

1. Introduction

Owing to its high efficiency, convection is a preferred heat-transfer mechanism in practical applications and in natural phenomena. In particular, it occurs in a wide variety of physical circumstances ranging from stellar activities in astrophysics to natural convection in the atmosphere and Earth's mantle (see, for example, Ahlers, Grossmann & Lohse 2009 and references therein). In spite of the great variety of practical examples, the essential features of thermal convection problems can be captured by an idealized model: a confined flow between highly conducting parallel plates heated from below and cooled from above. In this fluid layer, thermal expansion produces an unstable density gradient, which, if strong enough, generates a flow referred to as thermal convection or Rayleigh–Bénard convection (Bénard 1900; Rayleigh 1916). As the temperature difference is increased, the flow progressively evolves from a steady to an unsteady regime and eventually to turbulence. This paradigm of thermal convection is generally based on the Boussinesq approximation, in which the fluid properties are assumed to be constant despite the presence of temperature gradients, and the effect of the temperature in the momentum equation is accounted for only in the buoyancy term (see, for example, Tritton 1988).

Rayleigh and Prandtl numbers are the main dimensionless parameters governing the Rayleigh–Bénard convection, and are defined, respectively, as $Ra = g\alpha\Delta T h^3/(\nu\kappa)$ and $Pr = \nu/\kappa$, where g is the acceleration due to gravity, h is the fluid-layer depth, ΔT is the temperature difference, and α, ν and κ are the fluid properties, viz. the thermal expansion coefficient, the kinematic viscosity and the thermal diffusivity, respectively. In the presence of a laterally confined fluid layer, another important parameter can be the aspect ratio (Γ), which represents the ratio between the maximum horizontal extent of the system and its depth. Sometimes, especially for low and moderate values of Ra, details such as the geometry of the flow apparatus also seem to matter (Daya & Ecke 2001).

The Rayleigh number characterizes the strength of the thermal destabilization forcing with respect to a viscous stabilizing effect. The Rayleigh number is proportional to the third power of the fluid-layer thickness across which the temperature difference is established; therefore, real problems are generally characterized by very high values of Ra. Accordingly, experiments and numerical simulations have strived to reach the highest possible Ra values. This has been achieved at Prandtl numbers in the range $0.7 \leqslant Pr \leqslant 8$, which is typical of gases or common liquids such as water. In particular, using a very effective experimental technique to obtain an extensive range of Ra, the highest value reached in controlled environment was $Ra = 10^{17}$ (Niemela *et al.* 2000). This technique exploits the properties of cryogenic helium gas close to the critical point (Threlfall 1975).

There are, however, other kinds of 'fluids' characterized by very different values of Pr; for example, Earth's interior can have Pr varying from 10^{-2} up to 10^{20}, say. In particular, the Earth's mantle is characterized by very high Prandtl numbers ($Pr > 10^{20}$) and moderate Rayleigh numbers ($10^5 \lesssim Ra \lesssim 10^9$) (see, for example, Peltier 1989). The Prandtl number measures the propensity of the fluid to diffuse momentum in relation to heat, and determines the difference between velocity and temperature diffusive scales. The influence of the Prandtl number on thermal convection dynamics is difficult to investigate experimentally, as Pr can be substantially changed mainly by changing the fluid. Studies following this approach are those of Xia, Liam & Zhou (2002) and Ahlers & Xu (2001). A different strategy for varying Pr was used in Niemela *et al.* (2000), Niemela & Sreenivasan (2003), Roche *et al.* (2002) and Ashkenazi & Steinberg (1999). It consists of working close to the critical point of compressed gas. This technique enables the exploration of the influence of Pr variations at quite high Ra. However, in both strategies, complications arise from the great difficulty of maintaining the properties constant across the fluid depth, with consequent violation of the Boussinesq approximation, especially at high Pr.

Numerical simulations can overcome these issues, even if they face other kinds of difficulties such as adequate spatial resolution and the integration over sufficiently long time windows. Some numerical studies, solving the full three-dimensional problem, deal with varying Pr (Verzicco & Camussi 1999; Kerr & Herring 2000; Schmalzl, Breuer & Hansen 2002; Breuer *et al.* 2004; Calzavarini *et al.* 2005). Among these, only Verzicco & Camussi (1999) imposed the non-slip condition on all the walls, reproducing the same set-up as experiments. The no-slip condition on the horizontal plates and the free-slip condition on the sidewall were adopted by Breuer *et al.* (2004) and Kerr & Herring (2000), while all free-slip surfaces were implemented by Schmalzl *et al.* (2002). Periodic boundary conditions characterize the work of Calzavarini *et al.* (2005). A smaller number of studies concerns very high Pr. In particular, Breuer *et al.* (2004) and Schmalzl *et al.* (2002) simulated the convective flow up to $Pr = 100$, but limited to a fixed Ra. The other works were mainly focused on lower Pr regimes.

In this work, we report a numerical study on thermal convection for high Prandtl numbers and moderate Rayleigh numbers for a wide range of Pr and Ra (see figure 1). The upper bounds of the Ra–Pr interval explored were limited by computing resources. High-Pr simulations are challenging owing to the computational difficulties in simulating flows which are 'quasi-Stokes', characterized by very slow dynamics and generally strongly affected by numerical instabilities, and, at the same time, also owing to the need to use highly refined grids required for resolving the smallest scales of the temperature field. One generally deals with only one of these issues at a time, but in this kind of study, all are present simultaneously.

The aim of this study is to provide additional data in a range of Ra and Pr not yet adequately explored, and to contribute to the understanding of such a complex dynamical system, consisting of large-scale circulations and plume structures, viscous and thermal boundary layers, and apparently irregular turbulent motion. In particular, we report the behaviour of the Nusselt number (Nu). The Nusselt number is the ratio by which the heat flux is enhanced with respect to the conductive value, and it represents a principal diagnostic of thermal convection problems. At high Pr, generally a small dependence of Nu on Pr has been theoretically predicted (Shraiman & Siggia 1990; Grossmann & Lohse 2001) and empirically found (Verzicco & Camussi 1999; Xia *et al.* 2002), although there are some differences in the absolute strength of the Pr effect. In order to correctly capture this small dependence, particular care has been

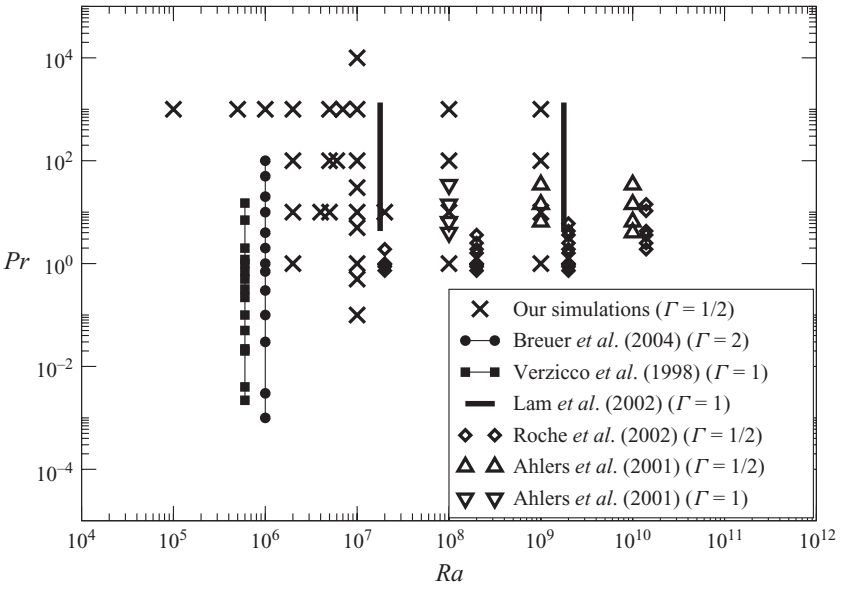

FIGURE 1. Map of performed simulations compared to the map of some recent numerical and experimental work at high Pr.

devoted to the choice of the grid size and to the evaluation of the errors affecting the data.

Since Nu is essentially determined by the drop of temperature close to the horizontal plates, the features of the thermal boundary layers represent a central issue in the investigation of the Nu behaviour. The role of the viscous boundary layers seems to be less fundamental. Indeed, even when free-slip conditions are imposed on the walls, convective phenomena still occur without significantly changing their characteristics (Verzicco 2003). However, when the no-slip condition is imposed on the walls, a viscous boundary layer develops. Its main effect is a reduction in the heat-transfer effectiveness (see figure 2 in Verzicco 2003). This implies that the viscous boundary layer influences the slope of the temperature profile at the wall, and therefore the thermal-boundary-layer features. We examine the relationship between viscous and thermal boundary layers by comparing their thicknesses for various Ra and Pr.

Before dealing with the boundary layers, the behaviour of the Reynolds number (Re) – and, consequently, of the Péclet number (Pe) – has to be analysed. In thermal convection, Re and Pe are outputs of the problem, since no typical velocity is imposed on the system. It is worth noting that their meaning here is more complex than usual, because the convective dynamics, and the corresponding characteristic velocities, derive from the combination of thermal and momentum dynamics, which can be driven by advective or diffusive features in different ways. For Pr of the order of unity, the typical large-scale velocities of the flow are scaled well by the free-fall velocity $U = \sqrt{g\alpha\Delta T h}$ (Prandtl 1952; Tritton 1988; Niemela *et al.* 2001; Verzicco & Camussi 2003; Brown & Ahlers 2009), which results from the balance between the inertial and buoyancy terms of the momentum equation. For high Prandtl numbers, however, the momentum tends to be very diffusive and inertial forces become small; accordingly, the present simulations at high Pr showed that U does not represent the typical velocity of the large-scale structure. By scaling the results, we have found that the large-scale characteristic velocity is $V = U/\sqrt{Pr}$, which

yields a more suitable non-dimensional form of the Boussinesq equations at high Pr. The corresponding estimate of the Reynolds number is $Re = Vh/\nu = \sqrt{Ra}/Pr$. As a consequence, the Péclet number, $Pe = Vh/\kappa = \sqrt{Ra}$, becomes independent of Pr. To verify the reliability of these estimates, the results of all the performed simulations have been analysed carefully.

In the range of Ra and Pr explored in this study, we found steady, periodic and turbulent solutions. The transition from one convective state to another represents an open and fascinating problem, especially in small-aspect-ratio cells ($\Gamma \lesssim 1$) where the flow structures strongly depend on system geometry. Almost all pattern-formation studies concern convective systems of large aspect ratio ($\Gamma \gg 1$) (Bodenschatz, Pesch & Ahlers 2000). For cells of moderate aspect ratio ($1 \lesssim \Gamma \lesssim 10$), a brief review, concerning the work on the early convective states, can been found in Boronska & Tuckerman (2006). Through experiments, numerical simulations and theoretical calculations, the work just cited mainly provides a stability analysis of convective states. In particular, it shows that the critical Ra for the onset of motion steeply increases above the theoretical value (obtained for $\Gamma \to \infty$) when Γ decreases below 2 (Charlson & Sani 1970). Other results are that non-axisymmetric motions appear in the early convective state when Γ is sufficiently small ($\Gamma \leqslant 1.6$) (Hardin & Sani 1993; Oresta, Stringano & Verzicco 2007); several different stable patterns are possible for the same final Ra and Pr (Hof, Lucas & Mullin 1999; Boronska & Tuckerman 2010); periodic behaviour occurs through a secondary bifurcation (Clever & Busse 1974; Croquette, Gal & Pocheau 1986; Rudiger & Feudel 2000). Our simulations support these findings. We propose a qualitative description of convective states and of flow patterns found in our simulations at a high Prandtl number. A rough estimate of the transition from a steady to an unsteady flow has been found in simulations close to this transitional regime, by monitoring the time evolution of the system. The main features of the convective structures of the unsteady solutions have been analysed through temperature and velocity-field visualizations.

This paper is organized as follows. The set-up of the problem, the grid-sizing criteria and the checks of the data set are presented in § 2. A qualitative picture of the transitional phases and the flow structures is provided in § 3. The Nusselt-number behaviour with respect to Ra and Pr is shown in § 4. In § 5 we discuss the characteristic velocity and show the Re and Pe behaviours. In § 6 we deal with the viscous- and thermal-boundary-layer thicknesses, their relation with respect to local and global definitions, their trends with respect to Ra and Pr, and to Re and Pe. Concluding remarks are given in § 7.

2. Numerical set-up

2.1. *Governing equations and numerical code*

The computational domain consists of a cylindrical cell of aspect ratio (i.e. ratio of the diameter to the cell height) $\Gamma = 1/2$. Cold and hot fixed temperatures are imposed on the top and the bottom plate, respectively. The sidewall is adiabatic and all the cell surfaces satisfy the no-slip condition. This set-up is the same as previous experiments (see, for example, Castaing *et al.* 1989; Niemela *et al.* 2000; Ahlers & Xu 2001; Niemela & Sreenivasan 2003 and Chavanne *et al.* 2001) and numerical works (see, for example, Verzicco & Camussi 1999, 2003), allowing a proper comparison of the results.

The flow is solved by the numerical integration of the three-dimensional time-dependent Navier–Stokes equations under the Boussinesq approximation. In

particular, the numerical code is based on the following non-dimensional form of the equations:

$$\left.\begin{aligned} \frac{\mathrm{D}\boldsymbol{u}}{\mathrm{D}t} &= -\nabla p + \Theta\hat{\boldsymbol{k}} + \left(\frac{Pr}{Ra}\right)^{1/2}\nabla^2\boldsymbol{u}, \quad \nabla\cdot\boldsymbol{u} = 0, \\ \frac{\mathrm{D}\Theta}{\mathrm{D}t} &= \frac{1}{(PrRa)^{1/2}}\nabla^2\Theta, \end{aligned}\right\} \tag{2.1}$$

where $\mathrm{D}/\mathrm{D}t = \partial/\partial t + \boldsymbol{u}\cdot\nabla$ is the material derivative, $\hat{\boldsymbol{k}}$ the unit vector pointing in the opposite direction with respect to gravity, $\boldsymbol{u}$ the velocity vector, p the pressure separated from its hydrostatic contribution and Θ the non-dimensional temperature. The equations have been made non-dimensional using the free-fall velocity $U = \sqrt{g\alpha\Delta T h}$, where h is the distance between hot and cold plates and their temperature difference is $\Delta T = T_h - T_c$; T_h is the temperature of the hot (bottom) plate and T_b is that of the cold (top) plate. The non-dimensional temperature Θ is defined by $\Theta = (T - T_c)/\Delta T$ and its range is $0 \leqslant \Theta \leqslant 1$. The dimensional temperature and velocity are indicated by T and $\boldsymbol{u}^*$, to distinguish them from their non-dimensional forms Θ and $\boldsymbol{u}$. Hereafter, the overbar denotes the time average; the spatial averages are indicated by $\langle\,\rangle_A$ and $\langle\,\rangle_V$ for area and volume averaging, respectively; the total average over time and space is denoted by $\langle\,\rangle$ without subscripts.

The Nusselt number is calculated by averaging in space and time the non-dimensional heat flux in the vertical direction, $Q_z = Q_z(\boldsymbol{x}, t)$, which is defined in terms of non-dimensional quantities as follows:

$$Q_z = -\frac{\partial\Theta}{\partial z} + Pe\Theta u_z. \tag{2.2}$$

In particular, $Nu = \langle\bar{Q}_z\rangle_A = \langle Q_z\rangle$, since the time-averaged heat flux must be constant across each horizontal section A.

Numerical simulations have been performed using the same code as in Verzicco & Camussi (2003). This code, written in cylindrical coordinates and based on a second-order finite-difference scheme, is described in detail in Verzicco & Orlandi (1996) and Verzicco & Camussi (1997). Actually, the code has been slightly improved with respect to its damping properties of the error propagation. The original time-scheme coefficients have been replaced by those proposed by Spalart & Moser (1991). This alteration was necessary to limit the strong numerical instabilities found to affect high-Pr simulations. (Details on this aspect can be found in Silano 2009.)

2.2. *Grid resolution*

The mesh size must be set to be of the same order as the smallest scale of the problem, these being the dissipative scales. Care has to be devoted to the boundary layers, which must be adequately resolved near the solid surfaces, and to possible thin flow structures (plumes) penetrating the bulk region, which need adequate grid resolution in the azimuthal direction also (Stevens, Verzicco & Lohse 2010).

High-Pr flows are generally characterized by high Péclet numbers (Pe) and small Reynolds numbers (Re), and so the temperature scales are expected to be much smaller than the velocity scales. Equivalently, the thermal-boundary-layer thickness (δ_T) is expected to be smaller than the viscous-boundary-layer thickness (δ_U); and the thermal dissipation scales are smaller than the viscous dissipation ones. We assumed that the Batchelor scale, $\eta_B = \eta Pr^{-1/2}$ (Batchelor 1959) – with η being the Kolmogorov scale (Kolmogorov 1941) – is the smallest temperature scale for convective flows at high Pr ($Pr \geqslant 1$). This assumption is motivated by the fact that the temperature

Ra	Nu	$\delta_{T_{rms}}/h$	η_B/h	n_θ	n_r	n_z	Δ_{min}	Δ_{mean}	Δ_{max}	$N_{\delta_{T_{rms}}}$
10^5	3.47 ± 0.01	0.1768	0.0450	109	18	70	0.0047	0.0111	0.0138	13
10^6	8.02 ± 0.08	0.0617	0.0195	101	25	101	0.0028	0.0089	0.0122	10
5×10^6	13.13 ± 0.16	0.0410	0.0114	101	25	101	0.0028	0.0089	0.0122	7
10^7	16.26 ± 0.17	0.0335	0.0090	129	31	136	0.0020	0.0069	0.0094	8
10^8	33.68 ± 0.20	0.0164	0.0042	385	81	321	0.0005	0.0026	0.0037	12
10^9	66.58 ± 1.59	0.0082	0.0020	385	81	321	0.0004	0.0025	0.0040	12

TABLE 1. *A posteriori* check of the grids. The values correspond to the actual solutions at $Pr = 10^3$. The Nusselt number Nu is reported together with its error bar. The thermal-boundary-layer thickness, $\delta_{T_{rms}}$, is derived from the root mean square (r.m.s.) of the temperature profile. The Batchelor scale η_B is calculated using the total dissipation rate $\langle\epsilon\rangle$. The number of grid points in the azimuthal, radial and vertical directions are, respectively, n_θ, n_r and n_z. The typical grid size is $\Delta = (2\pi r \Delta\theta \Delta r \Delta z)^{1/3}$, with Δ_{min}, Δ_{mean} and Δ_{max} corresponding to its minimum, mean and maximum values. $N_{\delta_{T_{rms}}}$ represents the number of points inside the thermal boundary layer.

(active scalar) seems to behave as a passive scalar at dissipative scales (Niemela *et al.* 2001; Zhou & Xia 2008). Thus, the grids were set for resolving the Batchelor scale in the bulk region. In agreement with the most accurate numerical works (Emran & Schumacher 2008; Shishkina & Wagner 2008; Shishkina & Thess 2009; Stevens *et al.* 2010), 7–15 points were clustered inside the thermal boundary layers. For the few simulations at $Pr < 1$, the Kolmogorov scale has been considered as limiting the resolution instead of the Batchelor scale, since in that case, the viscous dissipation scale is expected to be smaller than the thermal dissipation scale (Verzicco & Camussi 2003). Note that at $Pr < 1$, the Obukhoff–Corrsin scale, $\eta_C = \eta Pr^{-3/4}$, should represent the thermal dissipation scale instead of the Batchelor scale (Batchelor 1959). For the simulations at $Ra = 10^8$, a more uniform grid has been chosen, by increasing the relative number of points in the azimuthal direction with respect to the vertical direction, in order to correctly resolve the thin sheet-like structures characterizing the unsteady solutions at high Pr (see later). Because of computational constraints, the grids for simulations at $Ra = 10^9$ have been set with the same number of points as the grids for simulations at $Ra = 10^8$. Since the flow at higher Ra has thinner boundary layers, more points were clustered close to the walls in the former case. It is worth pointing out that the grid resolution at $Ra = 10^9$ is indeed adequate, since in Stevens *et al.* (2010), a mesh with a comparable number of points ($385 \times 97 \times 385$) was employed at $Ra = 2 \times 10^9$ and the results converged to those on a grid of size $513 \times 129 \times 513$.

The grids were generally chosen to be the same for $Pr \geqslant 1$. Indeed both the Batchelor scale and the thermal-boundary-layer thickness were expected to be almost independent of Pr for high Pr. These predictions were obtained by estimating the Batchelor scale and the thermal-boundary-layer thickness in terms of the Nusselt number:

$$\eta_B/h = (1/Ra(Nu-1))^{1/4}, \tag{2.3}$$

$$\delta_T/h = 1/(2Nu), \tag{2.4}$$

and taking into account that Nu is a very weak function of Pr for $Pr \gtrsim 1$ (Verzicco & Camussi 1999; Xia *et al.* 2002). The relationship (2.3) can be easily derived by substituting the exact relation $\langle\epsilon\rangle = (\nu^3 Ra/h^4 Pr^2)(Nu-1)$ (Shraiman & Siggia 1990) into the definition of the Batchelor scale, $\eta_B = (\nu^3/\langle\epsilon\rangle)^{1/4} Pr^{-1/2}$, where $\langle\epsilon\rangle$ is the

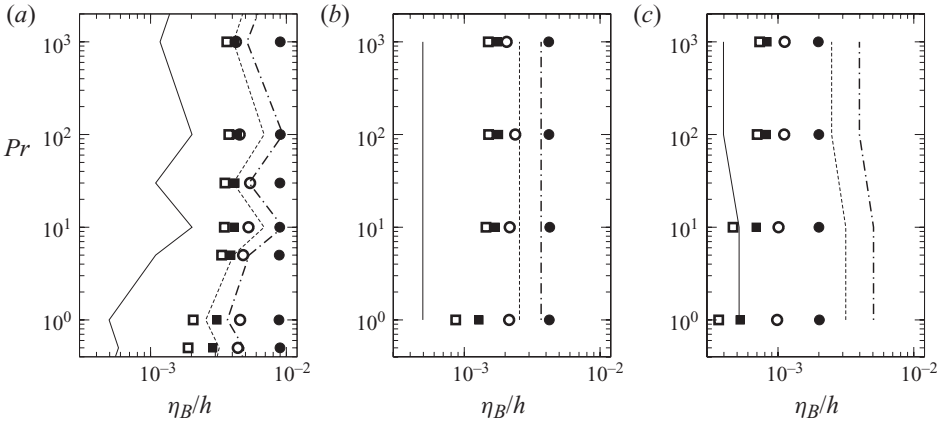

FIGURE 2. Batchelor scale as a function of Pr for $Ra = 10^7$ (a), $Ra = 10^8$ (b) and $Ra = 10^9$ (c). The Batchelor scale is calculated using different values of the viscous dissipation rate field $\varepsilon = \varepsilon(\boldsymbol{x}, t)$. Filled circles: total value $\langle\epsilon\rangle$; open circles: maximum value of the mean field $\max[\bar{\varepsilon}]$; filled squares: time-averaged peak value $\overline{\max[\varepsilon]}$; open squares: peak value $\max[\varepsilon]$. The solid line represents Δ_{min}, the dashed line indicates Δ_{mean} and the dotted–dashed line represents Δ_{max}.

total viscous dissipation rate. The relationship (2.4) holds exactly when the thermal-boundary-layer thickness is based on the tangent to the temperature profile (Ahlers, Grossmann & Lohse 2009). The relations (2.3) and (2.4) were used for the *a priori* estimate of the grid size. Table 1 lists the flow and grid parameters of the simulations.

The near independence of η_B/h and δ_T/h of Pr was confirmed by the actual results (figures 2 and 24). It is worth noting that the independence of the Batchelor scale with respect to Pr is basically valid even if other definitions of the dissipation rate are used to calculate the Batchelor scale. Even in the worst case of considering the peak dissipation values, a saturation value is reached for sufficiently high Pr. Moreover, the minimum local Batchelor scales (squares in figure 2) and the thermal-boundary-layer thicknesses (figure 24) slightly increase with increasing Pr before saturation, suggesting more constraining conditions in terms of grid resolution at $Pr \simeq 1$ rather than at higher Pr. This is somewhat counterintuitive since the common expectation is to have decreasing temperature scales for increasing Pr; indeed the Péclet number, $Pe = RePr$, is usually found to increase with Pr (see, for example, Grossmann & Lohse 2001 and Xia *et al.* 2002). However, one has to take into account that the Batchelor scale is based on the viscous dissipation rate $\varepsilon = \nu\,(\boldsymbol{\nabla u}^* : \boldsymbol{\nabla u}^*)$, while the dissipation of the temperature field is, in fact, measured by the thermal dissipation rate $\varepsilon_T = \kappa\,(\boldsymbol{\nabla} T \cdot \boldsymbol{\nabla} T)$. In spite of the strong relationship between the mean values ($\langle\epsilon\rangle$ and $\langle\epsilon_T\rangle$ are analytically related through the Nusselt number), the two dissipation fields do not seem to be connected locally. Indeed, in agreement with the results of Stevens *et al.* (2010), we found that peaks of ε_T are localized close to the top and bottom plates, while peaks of ε are also situated close to the sidewall (inset of figure 10c), where, in contrast, ε_T is quite small (inset of figure 9c).

The local disconnectedness between thermal and viscous dissipation rates could not be simply due to the strong anisotropy characterizing the flow and due to the presence of walls. Indeed, peaks of ε_T have also been found far from peaks of ε for passive scalar mixing in homogeneous and isotropic turbulent flows (Schumacher, Sreenivasan & Yeung 2005). An indication of the loose local correspondence between ε and ε_T is given

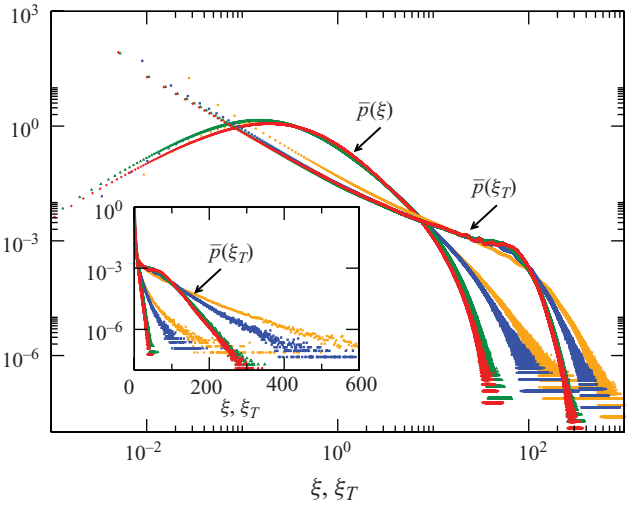

FIGURE 3. Probability density function averaged in time and calculated on the whole volume of the dissipation rates normalized by the mean values. The p.d.f. of viscous dissipation, $\xi = \varepsilon/\langle\epsilon\rangle$, and that of thermal dissipation, $\xi_T = \varepsilon_T/\langle\epsilon_T\rangle$, are calculated at $Ra = 10^9$ and varied Pr. Red: $Pr = 10^3$; green: $Pr = 10^2$; blue: $Pr = 10^1$; orange: $Pr = 10^0$. The inset shows the same curves plotted using a linear scale in the abscissa.

by the different shapes of their probability density functions (p.d.f.s) (see figure 3). This means that a local definition of the Batchelor scale is not useful for a comparison with the local grid size. (In a more general setting, the appropriateness of the Batchelor scale for high Prandtl numbers has been examined by Donzis, Sreenivasan & Yeung (2010).) For this reason, the data check is limited to global values, and the typical grid sizes shown in figure 2 (vertical lines) are significant only with respect to the global Batchelor scale (filled circles). Nevertheless, the data trends can give a qualitative indication on the correctness of the grid-sizing criteria adopted above. Figure 3 shows the p.d.f.s of the thermal and viscous dissipation fields at different Pr. The p.d.f.s, calculated on the whole volume and averaged in time, are performed with respect to normalized values, $\xi = \varepsilon/\langle\epsilon\rangle$ and $\xi_T = \varepsilon_T/\langle\epsilon_T\rangle$. The tail of the thermal-dissipation p.d.f. is less pronounced as Pr increases, following a similar relative behaviour of the tails of viscous dissipation p.d.f.s, indicating that, with increasing Pr, the simulations need less constraining requirements of grid resolutions. This is confirmed by the checks of the error affecting the Nusselt number. This error is defined as follows. The Nusselt number is calculated as the average of the values obtained in different ways: through its relationships with the viscous and thermal dissipation rates, averaging the non-dimensional heat flux in the vertical direction at each horizontal section of the cell, as well as in the whole volume. The difference between the maximum and the minimum of this set of values is considered to be the Nu error bar.

These error estimates represent a good check of the results, since the derivative fields are also involved. A similar check has been performed by Stevens *et al.* (2010), Verzicco & Camussi (2003) and Calzavarini *et al.* (2005). In our case, we obtain quite satisfactory results. Indeed, the Nu error bar is generally less than 3 % of the mean value. (For steady simulations, the error percentage decreases below 1 %.) Somewhat poorer results are obtained only at $Pr < 1$ ($Ra = 10^7$) and at $Ra = 10^9$. However, at $Ra = 10^9$, the error bar is less than or equal to 5 % except at $Pr = 1$. In this last case

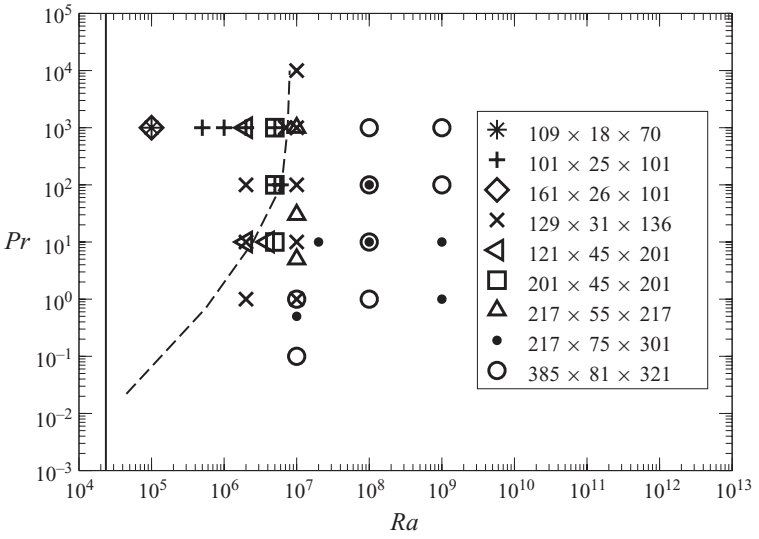

FIGURE 4. Map of simulations performed in a cylindrical cell of aspect ratio $\Gamma = 1/2$. The legend shows the corresponding number of grid points in the azimuthal, radial and vertical directions. The vertical solid line represents the critical Ra for the onset of convection (Oresta *et al.* 2007). The dashed line represents the threshold Ra to pass from a steady to an unsteady flow.

and for the two simulations at $Pr < 1$, the error bar is around 8–10 %. It is, however, at least three times smaller than the typical time variability of the Nu signal (the r.m.s. of Nu being around 30 % of the mean).

The above results are, however, self-referential. In fact, if the solutions are not correctly resolved, the results can be wrong and therefore also the check of the errors can be misleading. The only reliable check in order to assess the grid independence of the solutions is a grid-refinement analysis. It has been applied extensively (see figure 4), verifying that the results obtained with coarser grids are within the error bars of those of more refined grids. In cases for which it was not possible to evaluate an error bar, we required (somewhat arbitrarily but reasonably) the difference between the coarse and the refined grids results to be less than 5 %.

For the reference simulations at $Ra < 10^7$, it has been found that all the quantities shown in this paper differ by less than 3 % between the coarse and refined grids. The most critical simulations are, however, at higher Ra, where four reference simulations have been performed: at $Ra = 10^7$ and $Pr = 10^0, 10^3$ and at $Ra = 10^8$ and $Pr = 10^1, 10^2$. In these cases, differences equal to or smaller than 3 % have been found for all the mean values, the time-averaged peaks of the velocity components, and the r.m.s. values of Nu and velocities. For higher order quantities such as the values of the fluctuating dissipation rates, the relative error is of the order of 5 %. Table 2 summarizes the main grids involved in this analysis and shows the values of the Nusselt number calculated as the total average of the non-dimensional heat flux and the r.m.s. value of its time signal. Table 2 also shows the percentage of fluctuating dissipation rates with respect to the total dissipation rates. The fluctuating dissipation rates ϵ' and ϵ'_T are calculated by, respectively, using $\boldsymbol{u}' = \boldsymbol{u} - \bar{\boldsymbol{u}}$ and $\Theta' = \Theta - \bar{\Theta}$, representing the fluctuations of the velocity and temperature fields with respect to the mean flow.

Where available, the solutions obtained by the most refined grids have been used in the following analysis of the results.

Ra	Pr	n_{Tr}/n_{Tc}	n_θ	n_r	n_z	Nu	r.m.s.[Nu]	$\%\,\epsilon'/\langle\epsilon\rangle$	$\%\,\epsilon'_T/\langle\epsilon_T\rangle$
10^7	10^0	18.4	129	31	136	17.620	4.593	78.05	27.76
			385	81	321	17.639	4.531	78.25	27.93
10^7	10^3	4.8	129	31	136	16.264	1.461	5.57	2.94
			217	55	217	16.227	1.415	5.32	2.78
10^8	10^1	2.0	217	75	301	31.594	3.561	60.10	17.43
			385	81	321	31.507	3.584	59.82	17.38
10^8	10^2	2.0	217	75	301	33.408	2.164	73.37	15.55
			385	81	321	33.240	2.127	75.26	16.36

TABLE 2. Grid sensitivity. Comparison of coarse and refined grid results. The Nusselt number is calculated as $Nu = \langle Q_z \rangle$; r.m.s.[Nu] is the rms value of the Nu signal; ϵ' and ϵ'_T are the fluctuating dissipation rates; n_{Tr}/n_{Tc} is the ratio of the total number of grid points for refined and coarse grids.

2.3. *Time windows*

The simulations were generally started from previous solutions at lower Pr. The steady and periodic solutions were run until stable values of all the quantities were reached. In particular, the simulations were continued until the signal of the volume-averaged temperature, after reaching a constant value, maintained its first six digits unchanged for at least 100 convective times. The convective time is here taken as $\tau_c = \tau\sqrt{Pr}$, where $\tau = h/U$ is the free-fall time (see § 5 for details).

The remaining unsteady simulations have been run for sufficiently long time windows to obtain statistically converged quantities. In particular, after the initial transient, each simulation was continued for at least $500\,\tau_c$. This, however, represented a minimum requirement, because long-term phenomena appeared evident in the signal of volume-averaged temperature. So longer simulations, typically of the order of 1000–$2000\,\tau_c$, were performed with the aim of exploring this behaviour. In particular, at $Ra = 10^8$, long-period oscillations were found to arise in the volume-averaged temperature signal as Pr increases, while oscillations at convective time scale were found to smooth out (see figure 5). A discussion on this aspect is provided later in this paper.

In agreement with Oresta *et al.* (2007), the maximum time step was set at least 50 times smaller than the free-fall time ($\Delta t/\tau < 0.02$). However, this condition is generally far from the actual time-step size, which is much smaller (by one or two orders of magnitude, depending on the regime simulated) and determined by the stability condition of the time scheme of the code.

The computational limitations in this study were mainly due to the duration of simulations at high Pr rather than due to the grid size, which was kept almost the same for $Pr \geqslant 1$. Indeed, once the grid was fixed, obtaining a convective time unit for simulations at high Pr with respect to those at $Pr \simeq 1$ required a larger computational time. In particular, simulations at $Pr = 10^3$ were almost 30 times longer with respect to those at $Pr = 1$.

3. Transitional phases and flow structures

3.1. *A qualitative picture of transitions*

The fluid starts moving only when the destabilizing forces due to heating exceed the opposing viscous and thermal effects. The motionless state is stable only below a

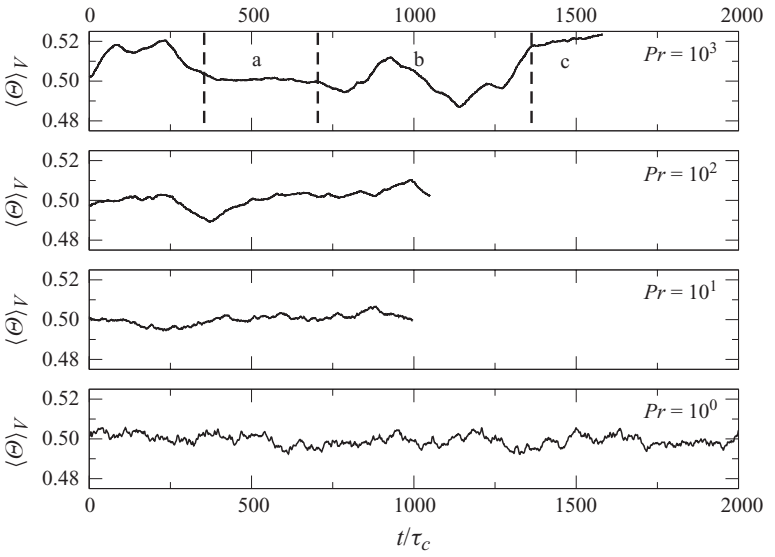

FIGURE 5. Signal of volume-averaged temperature at $Ra = 10^8$ for varied Pr. The signal shows long-term phenomena for large Pr.

critical Ra value, which depends on the aspect ratio Γ and the geometry of the cell, but is independent of Pr (Chandrasekar 1961). For a cylindrical cell with $\Gamma = 1/2$, the critical Ra is an order of magnitude higher than the theoretical value relative to an infinitely extended layer of fluid. Its estimate was numerically computed by Oresta *et al.* (2007): $Ra_C \simeq 2.35 \times 10^4$ (solid line in figure 4).

Above Ra_C, steady convective motions appear. In agreement with results concerning cells of high aspect ratio (Krishnamurti & Howard 1981), the steady state persists for a longer Ra interval as Pr increases. At $Pr = 10^3$ we found that the threshold value (Ra_U) for the transition from a steady to an unsteady flow is approximately equal to $Ra_U \approx 7.5 \times 10^6$ ($7 \times 10^6 < Ra_U < 8 \times 10^6$). A rough estimate of Ra_U was also obtained at lower Pr: $2 \times 10^6 < Ra_U < 3 \times 10^6$ at $Pr = 10$, and $5 \times 10^6 < Ra_U < 6 \times 10^6$ at $Pr = 10^2$. Using also the results of previous simulations performed by Oresta *et al.* (2007) at lower Pr, it was possible to derive an estimate of Ra_U on a wide range of Pr (dashed line in figure 4). In contrast to Ra_C for the onset of motion, Ra_U for the transition from a steady to an unsteady flow increases with Pr until a saturation value is attained for $Pr \gtrsim 10^2$.

In the range explored ($10 \leqslant Pr \leqslant 10^3$), the unsteady state appears as a locally periodic motion. This result agrees with the previous results obtained at lower Pr (Verzicco & Camussi 1997; Oresta *et al.* 2007). We distinguish between steady and periodic solutions by checking if the signals of local quantities are steady or periodic when the signal of the volume-averaged temperature reaches a steady state (figure 6), since the volume-averaged temperature signal is steady even when the flow is periodic. The identification of Ra_U is, however, only approximate since the closer the Ra is to Ra_U, the longer is the relaxation time of the system. This implies that very long simulations must be carried out in order to distinguish the slowly damped oscillations from the sustained ones. However, very precise calculations could be meaningless. Indeed, the strong sensitivity to the initial condition and to the grid size which generally affects these threshold values introduces a degree of uncertainty, which is unavoidable in this kind of approach.

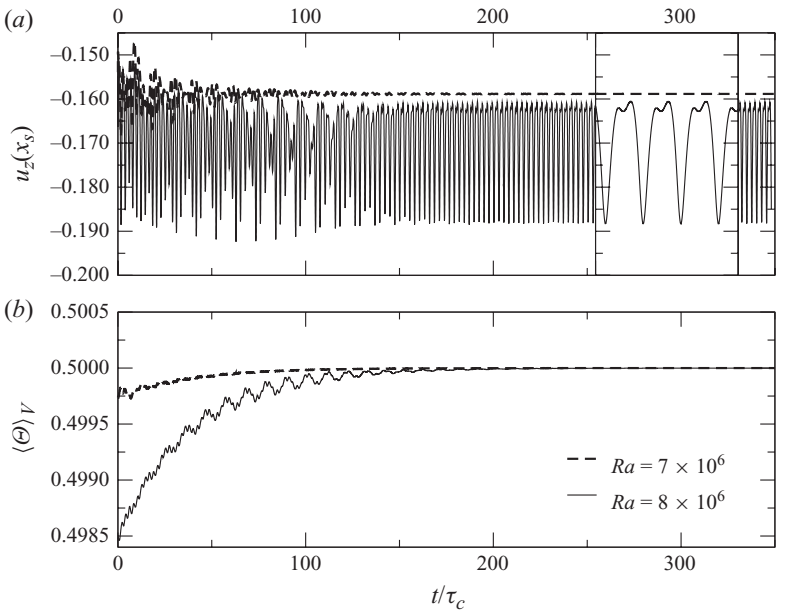

FIGURE 6. Time signals before and after the transition from the steady to the unsteady flow at $Pr = 10^3$. (*a*) Vertical velocity signal measured in an inner point x_s of the cell ($x_s = (\theta_s, r_s, z_s)$ with $\theta_s = 0$, $r_s = 0.2$ and $z = 0.1$). The inset is a zoom showing the time variation of the signal on an enlarged time scale. (*b*) Volume-averaged temperature signal. All the shown quantities are made non-dimensional according to (5.1).

With increasing Ra, the picture becomes less neat because the simulations are too sparse. One observes some isolated peaks in the spectrum of the Nusselt-number signal even in simulations which have lost periodicity features. Figure 7 shows the Nu signals and the corresponding spectra for the three unsteady solutions at $Pr = 10^3$. With increasing Ra, the spectra fill the gaps between the peaks until a continuous spectrum is obtained. Even at $Ra = 10^9$ and $Pr = 10^3$, the flow shows some turbulent features since the dissipation rate of the velocity fluctuations becomes the main contribution to the total viscous dissipation rate (figure 8*a*). Even the contribution of the fluctuations to the total heat flux dominates with respect to the mean flow contribution in the bulk region (figures 8*b* and 8*c*). The different shape of the profiles in figure 8(*c*) simply reflects the different mean flow structures found at different Pr (see § 3.2).

At $Pr = 10^3$ and $Ra = 10^8$, although the flow possesses detached plumes and an apparent degree of disordered motion (see later), the mean flow dominates with respect to the fluctuating component (figures 8*a* and 8*b*). At lower Pr, instead, the flow presents stronger turbulent features as Pr decreases. The scatter in the fluctuating dissipation rate with Pr in figure 8(*a*) is ascribed to the different mean flow structures, which affect the data trends especially at lower Ra.

Figure 8(*a*) shows that the main contribution to the thermal dissipation rate is due to the mean flow, even at the lowest Pr and the highest Ra, when the degree of turbulence should be higher. In particular, the largest contribution to the thermal dissipation comes from the regions close to the horizontal plates (figure 9*a*), because of the strong temperature gradients in the thermal boundary layers. The temperature fluctuations close to the plates are not very effective in terms of thermal dissipation

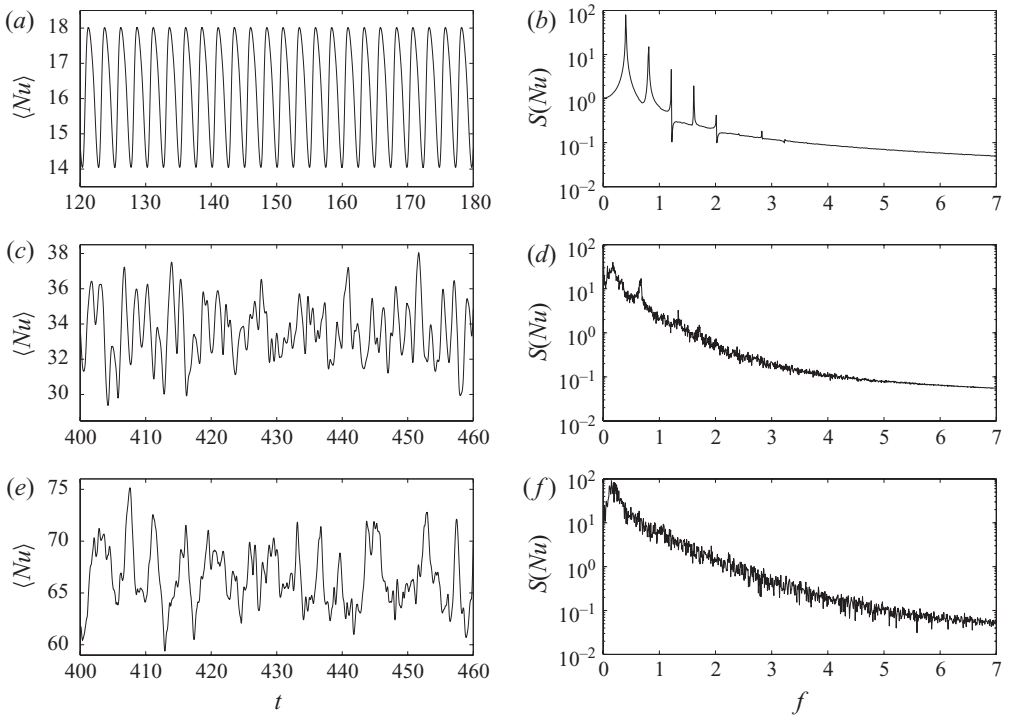

FIGURE 7. Bulk Nusselt-number signal and the corresponding spectrum. (*a*, *b*) $Ra = 10^7$; (*c*, *d*) $Ra = 10^8$; (*e*, *f*) $Ra = 10^9$.

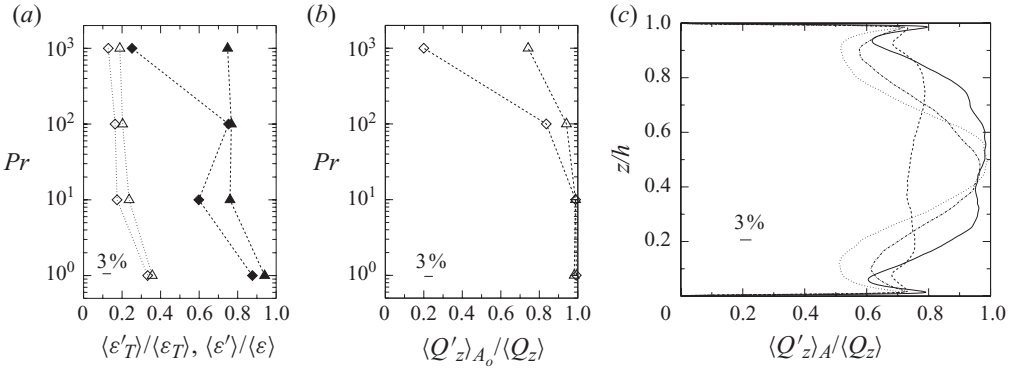

FIGURE 8. (*a*) Dissipation rates of velocity and temperature fluctuations, $\langle \epsilon' \rangle$ and $\langle \epsilon'_T \rangle$, with respect to the corresponding total dissipation rates, $\langle \epsilon \rangle$ and $\langle \epsilon_T \rangle$, as functions of Pr. Open symbols: $\langle \epsilon'_T \rangle / \langle \epsilon_T \rangle$; filled symbols: $\langle \epsilon' \rangle / \langle \epsilon \rangle$; diamonds: $Ra = 10^8$; upright triangles: $Ra = 10^9$. (*b*) Contribution to the total heat flux $\langle Q_z \rangle$ due to the velocity and temperature fluctuations ($\langle Q'_z \rangle_A = Pe \langle \overline{\Theta' u'_z} \rangle_A$) computed in the mid-plane A_o of the cell as a function of Pr. Diamonds: $Ra = 10^8$; upright triangles: $Ra = 10^9$. (*c*) Vertical profiles of the fluctuating heat flux at $Ra = 10^9$ and increasing Pr. Solid line: $Pr = 1$; dotted line: $Pr = 10$; dotted–dashed line: $Pr = 10^2$; dashed line: $Pr = 10^3$. In the panels a 3 % tic is reported that is an estimate of the error bar.

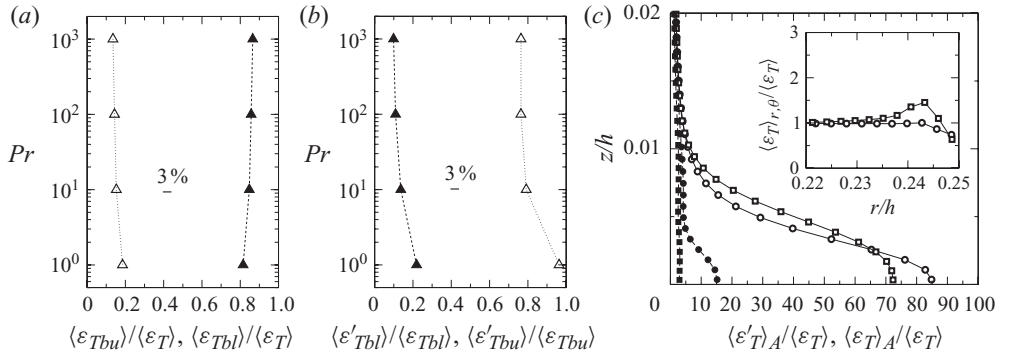

FIGURE 9. (*a*) Fraction of thermal dissipation rate which occurs in the bulk (open triangles) and close to the horizontal plates (filled triangles) at $Ra = 10^9$ and increasing Pr. The separation between the bulk and the thermal-boundary-layer region has been fixed at a distance of 1/50 of the cell depth from the top and the bottom plate, in a way to include the stronger thermal dissipation gradients in the thermal-boundary-layer region. It has been verified that moderate variations of this depth do not significantly affect the data trend. (*b*) Fraction of the turbulent thermal dissipation rate which occurs in the bulk (open triangles) and close to the horizontal plates (filled triangles) at $Ra = 10^9$ and increasing Pr. (*c*) Vertical profiles of the total thermal dissipation rate (open symbols) and of the turbulent thermal dissipation rate (filled symbols) at $Ra = 10^9$ and $Pr = 1$ (squares) and $Pr = 10^3$ (circles). Inset: corresponding horizontal profiles of the total thermal dissipation rate. In panels (*a*) and (*b*), a 3 % tic is reported that is an estimate of the error bar.

(figures 9*b* and 9*c*). On the contrary, in the bulk region, the thermal dissipation rate is mainly due to the temperature fluctuations (figure 9*b*).

In the case of the viscous dissipation rate, the fluctuating components of the flow produce a significant contribution not only in the bulk, where the largest part of the viscous dissipation occurs (figure 10*a*), but also very close to the walls (figures 10*b* and 10*c*). This implies a high effectiveness of the fluctuating component of the flow in the dissipation of the kinetic energy even in the viscous boundary layers, where the flow is generally considered to be laminar. The mean-flow effectiveness decreases with increasing Ra and decreasing Pr.

In conclusion, at sufficiently high Ra, the flow mainly behaves as turbulent in the bulk region both in the viscous and thermal dissipation rates while, close to the walls, it generally maintains turbulent-like features in the viscous dissipation rate and behaves laminar-like in the thermal dissipation rate.

3.2. *Flow structures and multiple solutions across transitional phases*

During the steady phase, the flow is characterized by different flow structures. In figure 11, the top row shows the typical patterns of the steady solutions at $Pr = 10^3$ and increasing Ra. After the onset of motion, the flow pattern is the same as for lower Pr (Verzicco & Camussi 1997): a single smooth roll filling the whole cell (figure 11*a*). The temperature iso-lines tend to be bent.

With increasing Ra, in addition to the single roll, smaller vortices appear at the edges of the top and bottom plates, and the big central roll appears deformed, like twisted in the azimuthal direction. The temperature iso-lines are no longer stratified (figure 11*b*). The single-roll structure deformed by an azimuthal torsion appears as one among many possible multiple steady solutions having a lower or a higher degree of deformation. Indeed, we found at $Ra = 2 \times 10^6$ and $Pr = 10^2$ two steady

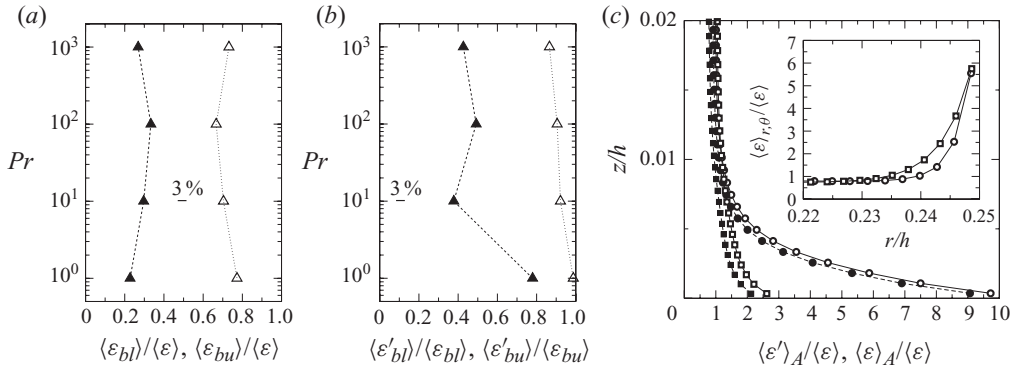

FIGURE 10. (*a*) Fraction of viscous dissipation rate which occurs in the bulk (open triangles) and close to the horizontal plates (filled triangles) at $Ra = 10^9$ and increasing Pr. The separation between the bulk and the thermal-boundary-layer region has been fixed at a distance of 1/50 of the cell depth from the top and the bottom plate and from the sidewall, in a way to include the stronger viscous dissipation gradients in the viscous-boundary-layer region. It has been verified that moderate variations of this depth do not significantly affect the data trend. (*b*) Fraction of the turbulent viscous dissipation rate which occurs in the bulk (open triangles) and close to the horizontal plates (filled triangles) at $Ra = 10^9$ and increasing Pr. (*c*) Vertical profiles of the total viscous dissipation rate (open symbols) and of the turbulent viscous dissipation rate (filled symbols) at $Ra = 10^9$ and $Pr = 1$ (squares) and $Pr = 10^3$ (circles). Inset: corresponding horizontal profiles of the total viscous dissipation rate. In panels (*a*) and (*b*), a 3 % tic is reported that is an estimate of the error bar.

solutions, mainly consisting of a single-roll structure, one with and the other without an azimuthal torsion. The same situation occurs at $Ra = 2 \times 10^6$ and $Pr = 10$. Checks performed using several grids and different initial conditions confirm these results. On the other hand, the possibility of multiple solutions has been widely verified by Boronska & Tuckerman (2010).

Before the onset of unsteady motion, the flow mainly consists of a single untwisted roll. The fluid temperature appears almost uniform in the bulk, while the hotter fluid rises along one side of the lateral wall and the colder fluid falls along the other (figure 11*c*). When the hotter and colder fluids meet at the edges of the plates, they form small eddies.

Increasing Ra further, there is a transition from the steady to unsteady flow. The unsteadiness at $Pr = 10^3$ appears in the flow as a couple of small hot and cold waves (hills) along the top and bottom plates. Travelling around the single-roll structure, they tend to detach along the sidewall forming hot and cold blobs, which force the formation of the subsequent couple of waves when they reach the corresponding opposite plate (figure 11*d*). With a slight increase in Ra, the blobs become more bulging. This travelling-wave phenomenon corresponds to local periodic solutions.

Following single-roll periodic solutions, at higher Ra, we found strongly three-dimensional structures different from single-roll structures. In particular, at $Pr < 10^2$, the solutions mainly show toroidal ring structures attached to the horizontal plates. At $Pr \gtrsim 10^2$, the simulations show structures mainly developing in the vertical direction. However, the instantaneous solutions are generally strongly unsteady and characterized by plume emissions (figures 11*e* and 11*f*). For $Pr = 1$, the temperature maps show plumes that randomly appear in various azimuthal positions on top and bottom plates (figure 12*a*). The flow is swept by unstructured recirculations, which

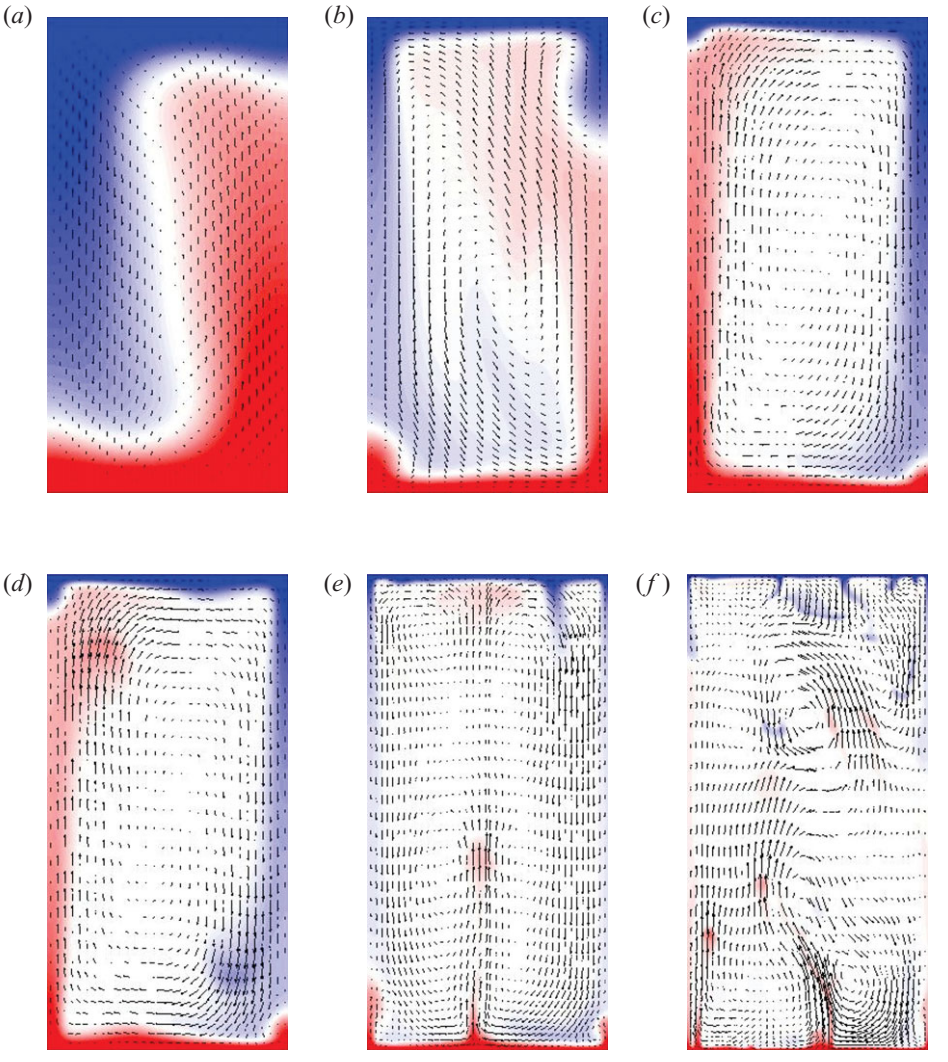

FIGURE 11. Flow structures at $Pr = 10^3$. (*a*) $Ra = 10^5$; (*b*) $Ra = 2 \times 10^6$; (*c*) $Ra = 7 \times 10^6$; (*d*) $Ra = 8 \times 10^6$; (*e*) $Ra = 10^8$; (*f*) $Ra = 10^9$. The colour map represents the temperature field and saturates at higher and lower temperatures: $0 \leqslant \Theta \leqslant 0.2$ (blue); $0.8 \leqslant \Theta \leqslant 1$ (red); $\Theta = 0.5$ (white); $0.2 < \Theta < 0.8$ (linear blue-white-red scale). The arrows show the velocity vectors tangent to the vertical section.

carry the hot and cold fluid portions up to the corresponding opposite plates mainly along the sidewall. The corresponding mean flow is axisymmetric, consisting of two toroidal structures, with the flow descending along the axis and ascending along the sidewall in the bottom half of the container, with the opposite in the top half. When averaged, the hot flow remains confined in the bottom half of the container and the cold flow in the top one. In contrast, at $Pr = 10^3$, the flow recirculations are driven by vertical jets fed by plumes detaching mainly from sheet-like structures and clustering in some nodal points (figure 12*b*). The plumes penetrate higher into the bulk region as Pr increases. The average effect is a mean flow which presents at higher Pr portions of the hottest (coldest) fluid close to the opposite cold top (hot bottom) plate.

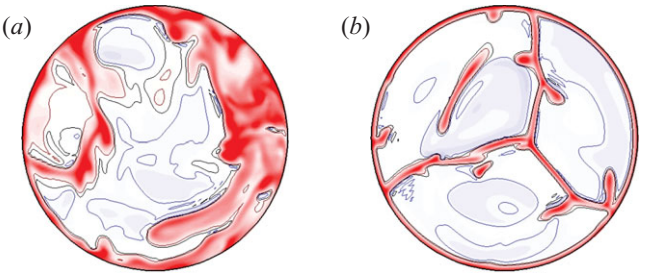

FIGURE 12. Flow structures at the horizontal sections close to the bottom plate for $Ra = 10^9$. (*a*) $Pr = 1$ and (*b*) $Pr = 10^3$. The colour map saturates at higher and lower temperature: $0 \leqslant \Theta \leqslant 0.2$ (blue); $0.8 \leqslant \Theta \leqslant 1$ (red); $\Theta = 0.5$ (white); $0.2 < \Theta < 0.8$ (linear blue-white-red scale). Black solid line: $\Theta = 0.5$.

The variety of these structures for increasing Ra affects the data trends, which generally show an irregular behaviour.

At $Ra = 10^8$ and $Pr = 10^3$, we found another example of multiple solutions, this time in the form of long-term variations. The main dynamics of the problem develop on the convective time scale, which is the typical scale of large flow circulation and plume detachment. Long-time phenomena, however, appear in some simulations, as already mentioned in § 2.3. In particular, the volume-averaged temperature signal shows anomalous variations on a time scale much longer than the convective time scale at $Ra = 10^8$ and increasing Pr (see figure 5).

At $Pr = 10^3$ and $Ra = 10^8$, the long-term variations in the volume-averaged temperature signal are more pronounced, and correspondingly we found different large-scale circulation structures. Roughly dividing the volume-averaged temperature signal into four time windows (top of figure 5), and neglecting the first interval that can be considered to be a transient, in the second time interval, the volume-averaged temperature is almost constant. During this interval, the flow is stably self-organized in a four-jet structure (figures 13*a* and 13*d*). In the next interval, the flow shows a more unstable behaviour, during which a six-jet structure prevails (figures 13*b* and 13*e*). In the last interval, the flow evolves into a nine-jet structure (figures 13*c* and 13*f*) which is quite stable in time.

Variations of the volume-averaged temperature signal with respect to the mean value of 1/2 indicate a breaking of symmetry in the temperature profile. At $Ra = 10^8$ and $Pr > 10^2$, the flow fluctuations become negligible with respect to the mean values (figures 8*a* and 8*b*). The large-scale structures are quite fixed in time, and the corresponding vertical profiles, when symmetric, remain so as well. If these structures destabilize, the recovery of the symmetry can be a long process owing to the prevailing diffusive dynamics of momentum with respect to advection (low Reynolds number). An interesting result is that, at $Ra = 10^8$ and $Pr = 10^3$, a quite stable and well-defined large-scale structure seems to be allowed with non-symmetric profiles (see figure 14). The figure shows the temperature profiles of the four-jet symmetric structure (solid lines) and of the nine-jet asymmetric structure (dashed lines).

The nine-jet structure is characterized by a 5 % positive shift of the central temperature with respect to the mean value of 1/2. This deviation is small but is beyond convergence errors concerning the total mean temperature. This structure is characterized by an ascending central jet which causes an asymmetry between the rising and descending flows (figure 13*f*). There already exist examples of axisymmetric problems in which the presence of a central jet induces a strong deviation (∼25 %)

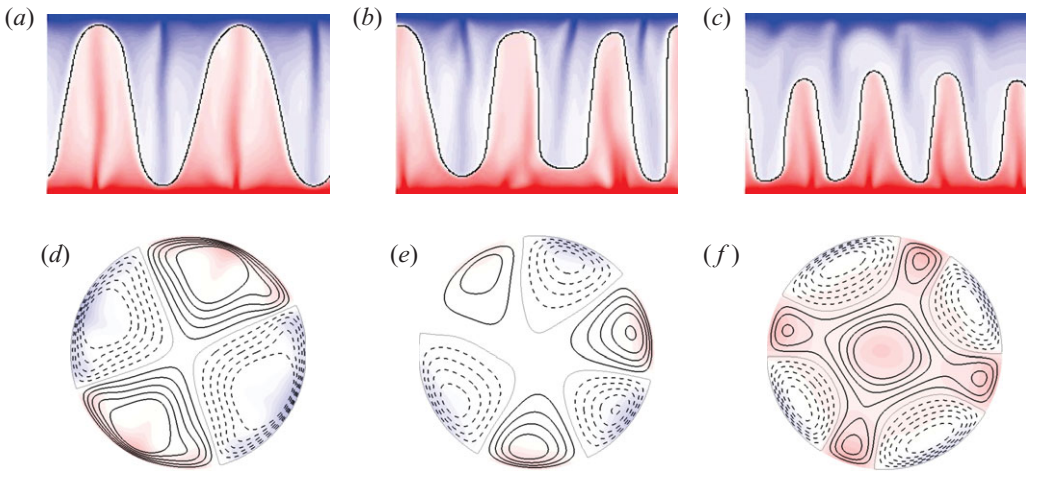

FIGURE 13. Multiple flow structures at $Ra = 10^8$ and $Pr = 10^3$. (*a*, *b* and *c*) The temperature map at the sidewall of typical snapshots, respectively, belonging to the time windows a, b and c of figure 5 (top). The cylindrical sidewall is unrolled with respect to the azimuthal direction obtaining two-dimensional plots. Black solid lines represent mean temperature iso-lines. (*d*, *e* and *f*) The mean-flow structures at the mid-plane obtained by averaging the time windows a, b and c of figure 5 (top). Solid lines: positive vertical velocity; dashed lines: negative vertical velocity; thin dotted lines: zero vertical velocity.

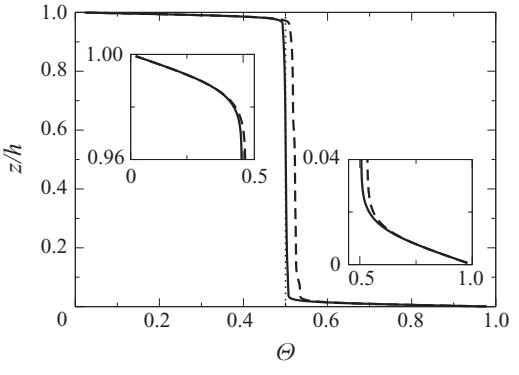

FIGURE 14. Temperature profiles of the four-jet structure (solid lines) and the nine-jet structure (dashed lines) at $Ra = 10^8$ and $Pr = 10^3$. Left inset: zoom at the top plate; right inset: zoom at the bottom plate.

of the central temperature from the mean value of the top and bottom temperatures (Umemura & Busse 1989). However, the case studied analytically by Umemura & Busse (1989) consists of a simplified structure, with an ascending (descending) central jet and a peripherally descending (ascending) jet, separated from each other by an isothermal core. The reason for the asymmetry is ascribed to the different heat transport mechanisms between the central and circumferential jets. The flow is strictly axisymmentric and governed by steady equations in the infinite *Pr* limit and with free-stress boundaries. In the present case, instead, the flow is unsteady, strongly three-dimensional and characterized by plume emission, and the physical arguments used by Umemura & Busse (1989) cannot be expected to apply to the present conditions, also because we obtain a positive deviation of the central temperature in the presence

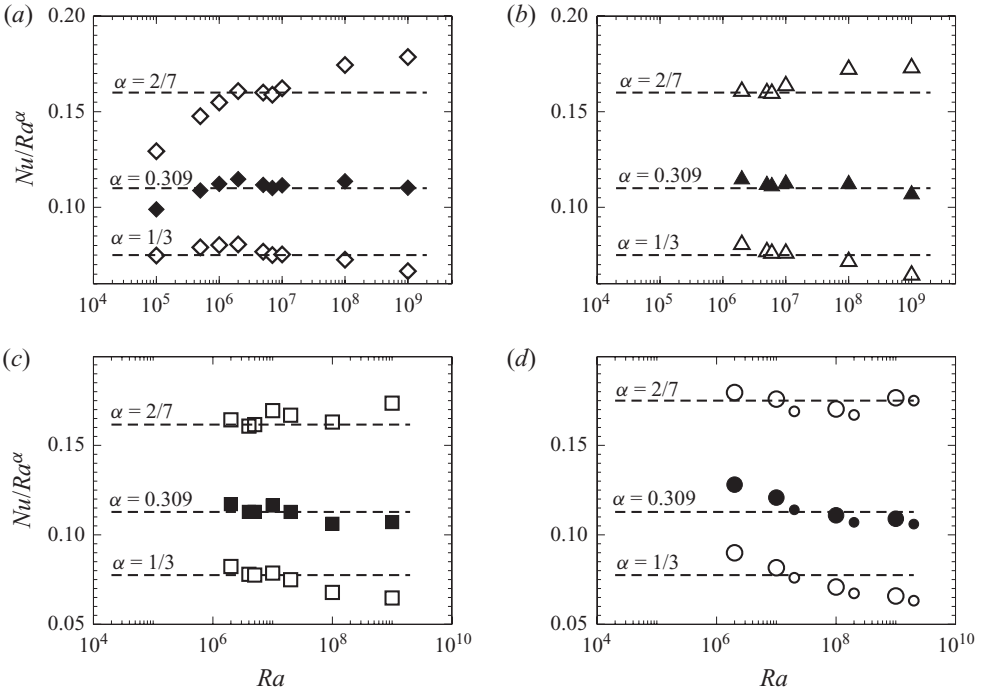

FIGURE 15. Nusselt number. (*a*) $Pr = 10^3$, (*b*) $Pr = 10^2$, (*c*) $Pr = 10$ and (*d*) $Pr = 1$. The smaller symbols in (*d*) correspond to the simulations performed by Stevens *et al.* (2010) at $Pr = 0.7$. The error bars are hidden by symbols.

of an ascending central jet. Furthermore, the strength of the phenomenon is much less pronounced in our case.

It is worth noting that, even if the central temperature of the nine-jet structure is shifted, its slopes approaching the top and bottom plates are basically the same as those of the temperature profile of the four-jet structure. This implies that the Nusselt number has to be the same. Also, in the other cases of multiple solutions, the discrepancies concerning the main quantities of interest are less than 5 % (inside the error bars). This represents an important issue, because the presence of different structures is often assumed to justify some scatter in data trends (Roche *et al.* 2002).

4. Nusselt number

Experimental results of Niemela *et al.* (2000) in a cell of aspect ratio $\Gamma = 1/2$, at $Pr \simeq 0.7$ and Ra spanning over 11 decades, show (to the zeroth order of approximation) a power-law exponent of 0.309. Our data seem to be consistent with these results, though differences arise when the Nusselt number is plotted in a compensated form (figure 15). These deviations are not surprising since, in the range of Ra and Pr considered, the flow passes through several transitional phases, and a single power law is expected to be inadequate to describe the Nu scaling in different regimes (Grossmann & Lohse 2000).

Larger deviations have been found at $Pr = 10^3$ (figure 15*a*), and at $Pr = 1$ (figure 15*d*). In the first case, for Ra before the transition from a steady to an unsteady flow ($Ra < 10^7$), the data are more consistent with a power law having exponent 1/3.

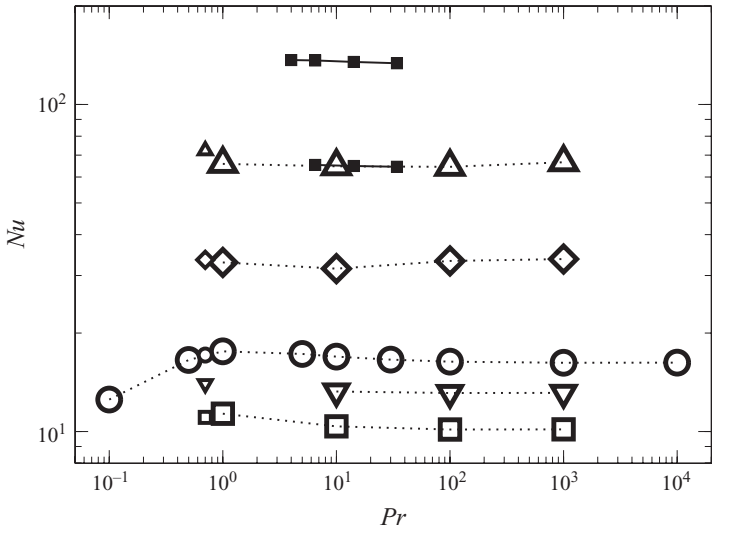

FIGURE 16. Nusselt number. Upright triangles: $Ra = 10^9$; diamonds: $Ra = 10^8$; circles: $Ra = 10^7$; inverted triangles: 5×10^6; and squares: 2×10^6. Small open symbols are extrapolated from Verzicco & Camussi (2003). Filled squares are extrapolated from Ahlers & Xu (2001). The error bars are hidden by the size of symbols.

This result agrees with previous data concerning the steady-flow regime (Heslot, Castaing & Libchaber 1987). Instead, for $Ra \geqslant 10^7$, the better correspondence is with the exponent 0.309 mentioned above. As expected from previous work (Verzicco & Camussi 2003; Castaing *et al.* 1989), in the case of $Pr = 1$, the data show a power-law exponent closer to 2/7 for $Ra \leqslant 10^8$. At higher Ra, our data are also consistent with the exponent 0.309, in agreement with the numerical results of Stevens *et al.* (2010).

The data are not sufficient to obtain precise values of the Nu–Ra exponent in the different regimes. However, the approximate value of 0.31, evaluated for the unsteady simulation at high Pr, can also be consistent with previous experimental results performed in similar Ra and Pr ranges (Ahlers & Xu 2001; Xia *et al.* 2002).

In the case of the dependence of Nu on Pr, figure 16 shows the trends of the data at fixed values of Ra. The Nusselt number for $Pr \gtrsim 1$ is essentially independent of Pr. At $Ra = 10^9$, the deviations from a constant value are less than 3.5 %, smaller than the error bar. These results agree with the experimental data of Ahlers & Xu (2001) (filled squares in figure 16). For lower Ra, the deviations increase as one approaches $Pr = 1$. However, they do not exceed 10 %. At $Ra = 10^7$, the Nu–Pr trend shows a small overshoot, while passing from low- to high-Pr regimes. A similar finding is shown in Grossmann & Lohse (2001). The slope at $Pr < 1$ is consistent with the exponent 0.14 found in Verzicco & Camussi (1999).

The independence of Nu with respect to Pr found in our simulations at $Ra = 10^9$ differs from the experimental results of Xia *et al.* (2002), obtained in a cell of aspect ratio $\Gamma = 1$ at similar Ra and Pr regimes. Their results show a slight decrease of Nu with increasing Pr, in agreement with the predictions of Grossmann & Lohse (2001). However, we should note that Nusselt numbers in cells of $\Gamma = 1$ and $\Gamma = 1/2$ show slightly different behaviours (Niemela & Sreenivasan 2003).

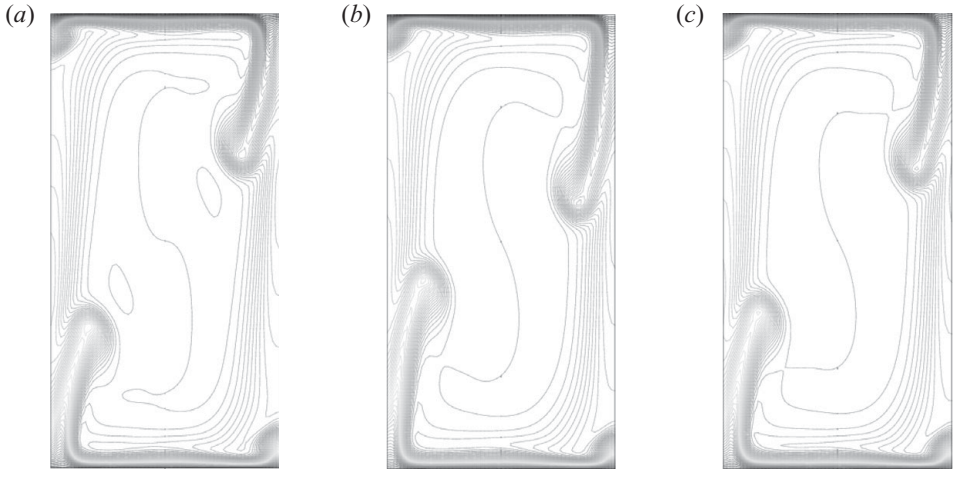

FIGURE 17. Isothermal lines of instantaneous temperature fields at $Ra = 10^7$ and (*a*) $Pr = 10^2$, (*b*) $Pr = 10^3$ and (*c*) $Pr = 10^4$.

5. Reynolds and Péclet numbers

5.1. *The non-dimensional form for large Pr*

The inadequacy of the free-fall velocity U, and the corresponding time $\tau = h/U$, to represent the characteristic large-scale dynamics at high Pr was especially evident in the periodic solutions obtained at fixed $Ra = 10^7$ and $Pr \geqslant 10^2$. Indeed, by monitoring time signals, we found that the corresponding period, which represents the convective dynamics well, is much longer than τ and increases strongly with Pr. In particular, we found that, for these periodic solutions, the whole temperature and pressure-gradient fields are essentially the same, while the velocity field may vary by several orders of magnitude in strength while maintaining the same shape. It is worth noting that this similarity prevails at each time step, not simply on the average (figure 17).

Practically, if temperature Θ_1, velocity $\boldsymbol{u}_1$ and pressure p_1 are the fields solved at $Pr = Pr_1 \geqslant 10^2$, and Θ_2, $\boldsymbol{u}_2$, p_2 those at $Pr = Pr_2 \geqslant 10^2 \neq Pr_1$, the simulations show that $\Theta_2 \backsimeq \Theta_1$, $\nabla p_2 \backsimeq \nabla p_1$ and $\boldsymbol{u}_2 \backsimeq a\boldsymbol{u}_1$, where a is a constant to be determined.

Thus, if $\Theta_1, \boldsymbol{u}_1, p_1$ are solutions of (2.1), then $\Theta_2 = \Theta_1, \boldsymbol{u}_2 = a\boldsymbol{u}_1$ and $p_2 = p_1 + f(t)$ are also solutions of (2.1) only if $t_2 = t_1/a$, $Ra_2 = Ra_1$, $a = \sqrt{Pr_1/Pr_2}$ and the advective term $\mathrm{D}\boldsymbol{u}/\mathrm{D}t$ of the momentum equation is equal to zero. These conditions are easy to derive by putting Θ_1, $\boldsymbol{u}_1$, p_1 and Θ_2, $\boldsymbol{u}_2$, p_2 in (2.1) and comparing the results.

This exercise shows some interesting features: for $Ra = 10^7$ and $Pr \geqslant 10^2$, the advective term $\mathrm{D}\boldsymbol{u}/\mathrm{D}t$ is quite negligible and the solutions are close to the infinite-Pr limit. The condition $Ra_2 = Ra_1$ indicates that this kind of similarity is possible only at fixed Rayleigh numbers, while $t_2 = t_1/a$ simply means that the time scales as the inverse of the velocity. The condition $a = \sqrt{Pr_1/Pr_2}$ suggests the proper way to make the equations non-dimensional.

Indeed, it is possible to define a new non-dimensional velocity as $\boldsymbol{v} = \sqrt{Pr}\boldsymbol{u}$ such that $\boldsymbol{v}_1 = \sqrt{Pr_1}\boldsymbol{u}_1 = \sqrt{Pr_2}\boldsymbol{u}_2 = \boldsymbol{v}_2$. As a consequence, the characteristic velocity will be $V = U/\sqrt{Pr}$, where U is the free-fall velocity. Using V instead of U to make the

Boussinesq equations non-dimensional, (2.1) are changed to

$$\left.\begin{aligned} \frac{1}{Pr}\frac{\mathrm{D}\boldsymbol{v}}{\mathrm{D}\mathfrak{t}} &= -\boldsymbol{\nabla} p + \Theta\hat{\boldsymbol{k}} + \frac{1}{\sqrt{Ra}}\nabla^2\boldsymbol{v}, \quad \boldsymbol{\nabla}\cdot\boldsymbol{v} = 0, \\ \frac{\mathrm{D}\Theta}{\mathrm{D}\mathfrak{t}} &= \frac{1}{\sqrt{Ra}}\nabla^2\Theta. \end{aligned}\right\} \tag{5.1}$$

Non-dimensional temperature and pressure in (5.1) are the same as in (2.1), while non-dimensional velocity $\boldsymbol{v}$ and time $\mathfrak{t}$, respectively, differ from $\boldsymbol{u}$ and t. Note that for $Pr = 1$, (2.1) and (5.1) are the same.

The set of equations (5.1) explicitly shows that in the high-Pr limit the convective dynamics are independent of Pr. There are, however, two more common non-dimensional forms that have the same feature and are consistent with the similarity of solutions at $Ra = 10^7$ and $Pr \geqslant 10^2$, and could be used instead of the form (5.1). They are based on the same length scale h, temperature scale ΔT and pressure scale $\Pi = \rho\alpha g \Delta T h$ as (2.1) and (5.1). The only differences are on the velocity scales and, as a consequence, on the time scales. One of these non-dimensional forms, largely used in theoretical work, is one in which the characteristic velocity U_κ is obtained by comparing the advective and the diffusive term of the temperature equation: $U_\kappa = \kappa/h = U/\sqrt{Pr\,Ra}$. The second one uses the characteristic velocity $U_\nu = \alpha g \Delta T h^2/\nu = U/\sqrt{Pr/Ra}$, which appears by comparing the buoyancy term to the diffusive term of the momentum equation. Note that these diffusive velocities include the same $\sqrt{Pr}$ correction to the free-fall velocity U as the above velocity V. However, they also modify their dependence on Ra with respect to U.

The only open issue in deciding the suitable form of the equations at large Pr is the choice of the characteristic velocity, since the other quantities are based on the same scales. This issue will be considered below.

5.2. *Characteristic velocity*

The proper characteristic velocity should be able to capture the main strength of the velocity field. Therefore, typical values of the actual velocities should be reasonably constant and of the order unity when non-dimensionalized by the characteristic velocity scale.

Considering the time-averaged peak vertical velocity $w_{peak} = \overline{\max[u_z^*]}$ as typical of the convective flow, figure 18 shows the four non-dimensional versions of this velocity as a function of Pr and for various Ra. Figure 18(*a*) shows that when the free-fall velocity $U = \sqrt{\alpha g \Delta T h}$ is used to make w_{peak} non-dimensional, a strong dependence on Pr arises. Instead, using the other three characteristic velocities mentioned above, there is some dependence on Pr which tends to disappear as Pr increases (figures 18*b*, 18*c* and 18*d*). Plotting the same values as a function of Ra (figure 19), one can see that the characteristic diffusive velocities $U_\kappa = \kappa/h$ and $U_\nu = \alpha g \Delta T h^2/\nu$ also yield a strong dependence on Ra (figures 19*c* and 19*d*). This dependence is reduced significantly for $V = U/\sqrt{Pr}$ (figures 19*a* and 19*b*). From these plots, it also follows that the characteristic velocity V leads to a weak dependence of the non-dimensional form of w_{peak} both on Pr and Ra at the same time. The same scenario holds if other velocities are considered as typical of the convective dynamics instead of w_{peak}. From these considerations, it appears that the characteristic velocity V and the corresponding non-dimensional form of (5.1) are most suitable to describe the dependence of the flow on Ra and Pr in the $Pr \gg 1$ regimes. It is evident from figures 18(*b*) and 19(*b*) that corrections to V are necessary to obtain a precise collapse of the curves onto a straight line. The corrections, however, strongly depend on the kind of velocity

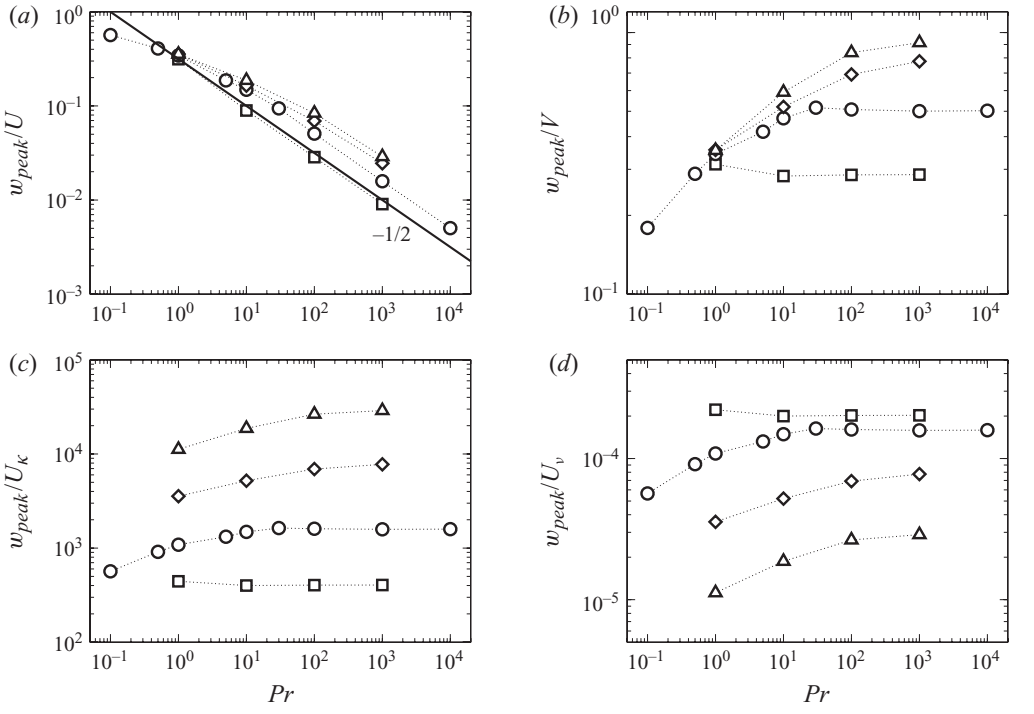

FIGURE 18. Peak vertical velocity as a function of Pr. (*a*) $U=\sqrt{\alpha g\Delta T h}$, (*b*) $V=\sqrt{\alpha g\Delta T h/Pr}$, (*c*) $U_\kappa=\kappa/h$ and (*d*) $U_\nu=\alpha g\Delta T h^2/\nu$. Squares: $Ra=2\times10^6$; circles: $Ra=10^7$; diamonds: $Ra=10^8$; and upright triangles: $Ra=10^9$.

considered as typical of the flow. Indeed, several choices are possible, and, even fixing a velocity, the corrections depend on the particular values of Ra and Pr when $Pr\neq1$. In figures 20(*a*) and 20(*b*), for example, the velocity considered is that corresponding to the maximum value of the r.m.s. horizontal velocity profiles. In this case, the behaviour is not monotonic with respect to Pr and Ra, implying that the corrections also change qualitatively.

For completeness, we show in figures 20(*c*) and 20(*d*) the behaviour of the temperature fluctuations corresponding to the maximum value of the r.m.s. temperature profiles as a function of Pr and Ra. In this case, the temperature fluctuations essentially scale with $\Delta T=T_h-T_c$ since the dependence on Pr and Ra is very weak (power-law exponents in absolute value smaller than 0.08) and can be considered a second-order effect.

5.3. *Reynolds and Péclet numbers*

Using the characteristic velocity $V=U/\sqrt{Pr}$, an estimate of the Reynolds number is $Re\sim\sqrt{Ra}/Pr$ and, consequently, $Pe\sim\sqrt{Ra}$, which is independent of Pr. More precise estimates need the same corrections valid for the characteristic velocity and imply identical uncertainties, since the actual Reynolds number is given by $Re(u^*/V)$, where Re is based on V and u^* is an actual typical velocity of the flow.

Figure 21 shows the actual values of Re compensated by Pr^{-1}, this being equal to Pe, as a function of Ra and Pr. In figures 21(*a*) and 21(*b*), the Reynolds number is based on time-averaged peak vertical velocity. Instead, in figures 21(*c*) and 21(*d*), it is based on the maximum value of the r.m.s. profile of the horizontal velocity.

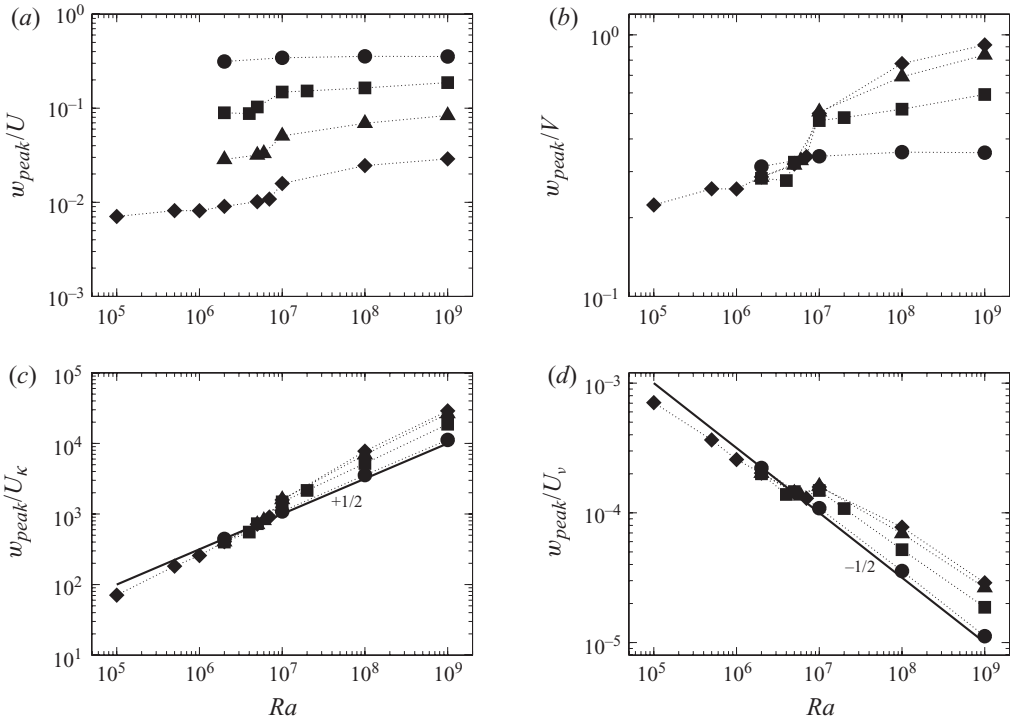

FIGURE 19. Peak vertical velocity as a function of Ra. (a), (b), (c) and (d) as figure 18. Circles: $Pr = 10^0$; squares: $Pr = 10^1$; upright triangles: $Pr = 10^2$; diamonds: $Pr = 10^3$.

Figures 21(a) and 21(c) include the best exponents of a power-law fitting for Re (and Pe) values versus Ra. Steady and unsteady solutions are considered separately. For high Pr, the exponent is higher than the estimated value of 1/2. The maximum departure is at $Pr = 10^3$ and $Ra \geqslant 10^7$ in the case of the peak vertical velocity (figure 21a), where the actual exponent is 25 % higher than 1/2. The growth of the exponent with increasing Pr is qualitatively in agreement with previous experimental results (Lam *et al.* 2002). However, the best correction (to the 1/2 power) is logarithmic. For high Pr, it implies that $Re/Pr^{-1} \sim \sqrt{Ra}\log Ra^{\alpha_s}$. In this case, the relative corrections with respect to the expected values (the absolute values, not the exponents) are less than 50 %, with an error growth much smaller than that resulting from the power-law fit of the actual data. Experimental results show a transition around $Ra = 10^7$–10^9, after which $Re \sim \sqrt{Ra}$ (without considering the dependence on Pr) (Lam *et al.* 2002; Brown, Funfschilling & Ahlers 2007). For high enough Rayleigh numbers, no corrections should be necessary but such a transition is not visible in our simulations.

Figures 21(b) and 21(d) show the behaviour of Re/Pr^{-1}, and therefore, of Pe, with respect to Pr at different values of Ra. For each fixed Ra, the data tend to approach constant values as Pr increases. For $Pr \geqslant 10^2$, the deviation from a constant trend is less than 3.6 %. We expect that the Péclet number becomes independent of Pr when the Reynolds number decreases below the critical limit represented by a solid line in figure 21(b). (For more details, see the next section.)

At lower Pr (in the region on the left of the solid line), the deviations from the scaling Pr^{-1} can exceed 50 %, depending strongly on Ra and on the kind of velocity

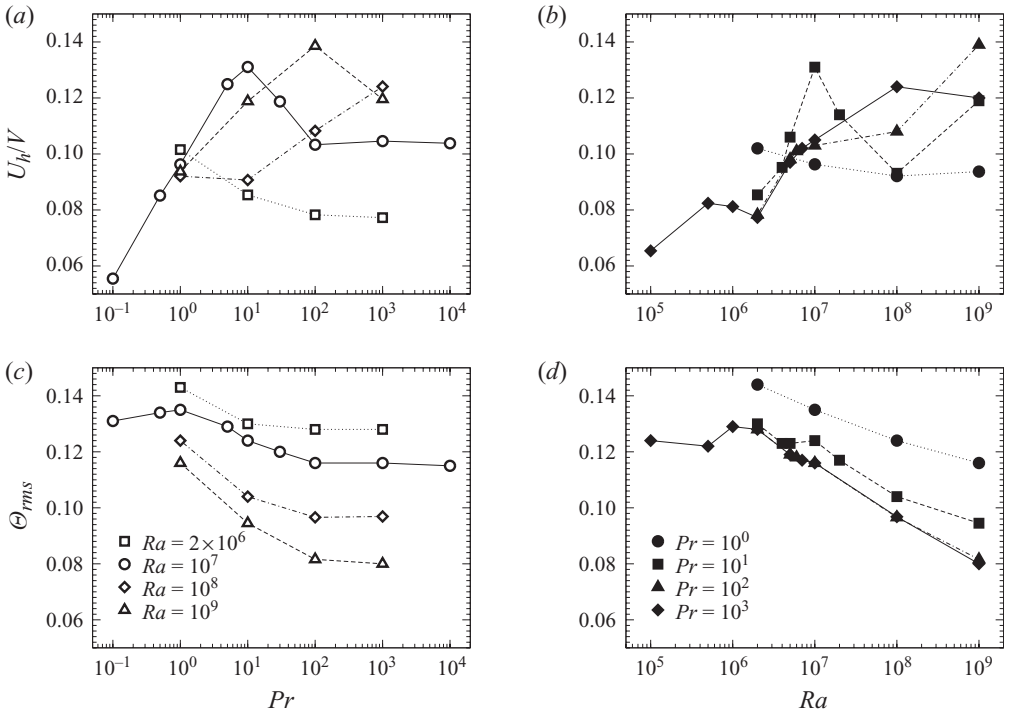

FIGURE 20. (*a*, *b*) Maximum value of the r.m.s. horizontal velocity profiles as a function of *Pr* and *Ra*, respectively. These values are made non-dimensional using the characteristic velocity $V = U/\sqrt{Pr}$. (*c*, *d*) Maximum value of the r.m.s. temperature profiles as a function of *Pr* and *Ra*, respectively. These values are non-dimensional according to the non-dimensional temperature Θ (see § 2.1). The symbols in (*a*) and (*b*) have the same meaning as those in (*c*) and (*d*), respectively.

considered. In particular, in the case of *Re* based on the peak vertical velocity (figure 21*b*), the deviation increases with increasing *Ra*. If we consider *Pe* instead of *Re*, the former slightly increases with increasing *Pr* before reaching a saturation, at least for sufficiently high *Ra*.

For $Ra = 10^7$ and $Pr \leqslant 1$, the power-law dependence of *Re* on *Pr* is approximately $Re \sim Pr^{-0.71}$. This is consistent with the results of Verzicco & Camussi (1999). At $Ra = 6 \times 10^5$ and in a cell of aspect ratio $\Gamma = 1$, these authors found an exponent varying from -0.73 to -0.94 when *Pr* increases. The exponent -0.7 was also found by Niemela & Sreenivasan (2003). They plotted the trend of *Re* versus *Pr* over a wide interval of *Pr* ($0.02 \lesssim Pr \lesssim 200$), using data from experiments of different authors. The aspect ratio varied between 1/2 and 1, and some data were extrapolated by holding *Ra* fixed at 10^{10}. Instead, the data of experiments by Xia *et al.* (2002) showed an exponent of -0.95 for high-*Pr* regimes ($10 \lesssim Pr \lesssim 10^3$), in a cell with $\Gamma = 1$, and *Ra* between 10^8 and 10^{10}.

These results seem to confirm the presence of a low-*Pr* regime, where approximately $Re \sim Pr^{-0.7}$, and a saturation regime at very high *Pr* ($Pr \gtrsim 10^2$), where $Re \sim Pr^{-1}$. The transition from one regime to another also seems to depend, apart from Rayleigh and Prandtl numbers, on the aspect ratio of the cell. A smooth approach to the saturation regime, as shown by our data, implying high uncertainty in the data fit, could explain the discrepancy in the scaling exponents found by the different authors.

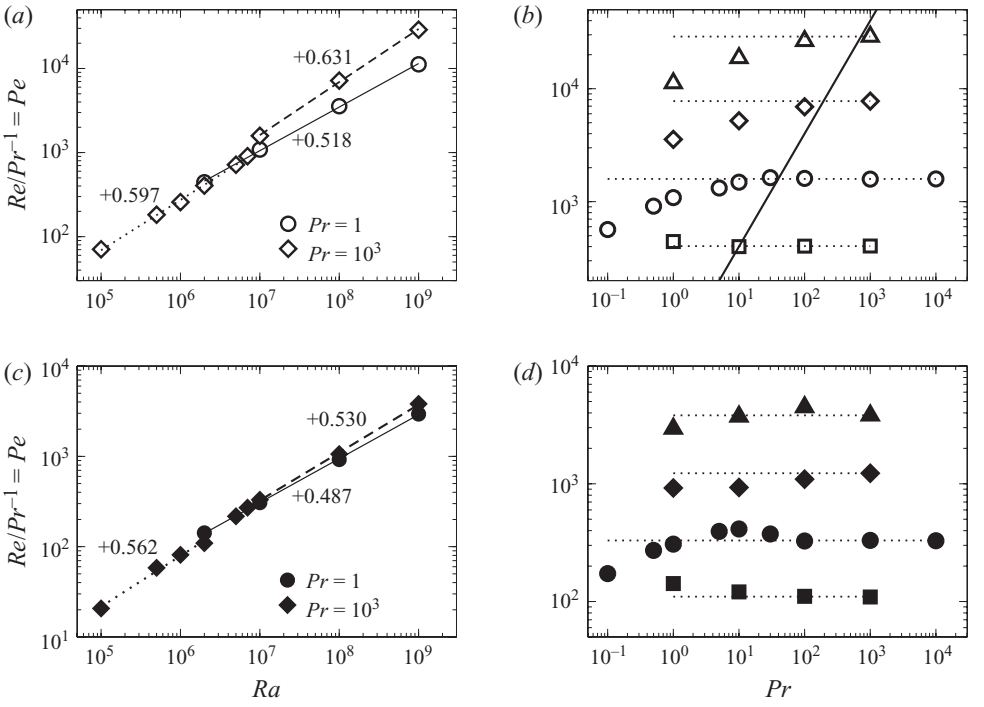

FIGURE 21. Re divided by Pr^{-1} calculated using the time-averaged peak vertical velocity (open symbols) and the maximum value of the r.m.s. horizontal velocity profile (filled symbols). In (b) and (d), squares: $Ra = 2 \times 10^6$; circles: $Ra = 10^7$; diamonds: $Ra = 10^8$; upright triangles: $Ra = 10^9$. In (b) the solid line represents $Re \simeq 40$, which is the saturation limit mentioned in § 6.

6. Boundary layers

6.1. *Boundary-layer thicknesses versus Pr and Ra*

Figure 22 shows the global profiles (i.e. averaged in time and over the horizontal sections) of the r.m.s. of the horizontal velocity at fixed $Pr = 1$ and increasing Ra (figures 22a and 22b), and at fixed $Ra = 10^9$ and increasing Pr (figures 22c and 22d). These profiles vary from one flow regime to another, depending on the mean flow structures and on Ra and Pr. The global profiles of the temperature r.m.s., in general, show a more regular shape, both with respect to Ra (figures 23a and 23b) and with respect to Pr (figures 23c and 23d). In the following discussion we use the height corresponding to the peak values of these profiles to define the viscous- and the thermal-boundary-layer thickness, respectively. In the next section (§ 6.2), we compare the main features of these global profiles with those of the corresponding local ones.

In agreement with the Nusselt-number behaviour, low sensitivity to the Prandtl number has also been found in the thermal-boundary-layer thickness (δ_T) for $Pr > 1$. In particular, δ_T, based on the time-averaged temperature–r.m.s. profile, slightly increases with Pr, eventually approaching a constant value (open symbols in figure 24). The independence of δ_T, and of Nu, of Pr for $Pr \gg 1$, is a consequence of the saturation of the viscous-boundary-layer thickness (δ_U) with increasing Pr (filled symbols in figure 24). The saturation of the viscous-boundary-layer thickness is due to the fact that δ_U cannot indefinitely grow as Re decreases (Pr increases), at least because the cell has a finite size. Figure 25(a) shows δ_U as a function of Re. The δ_U

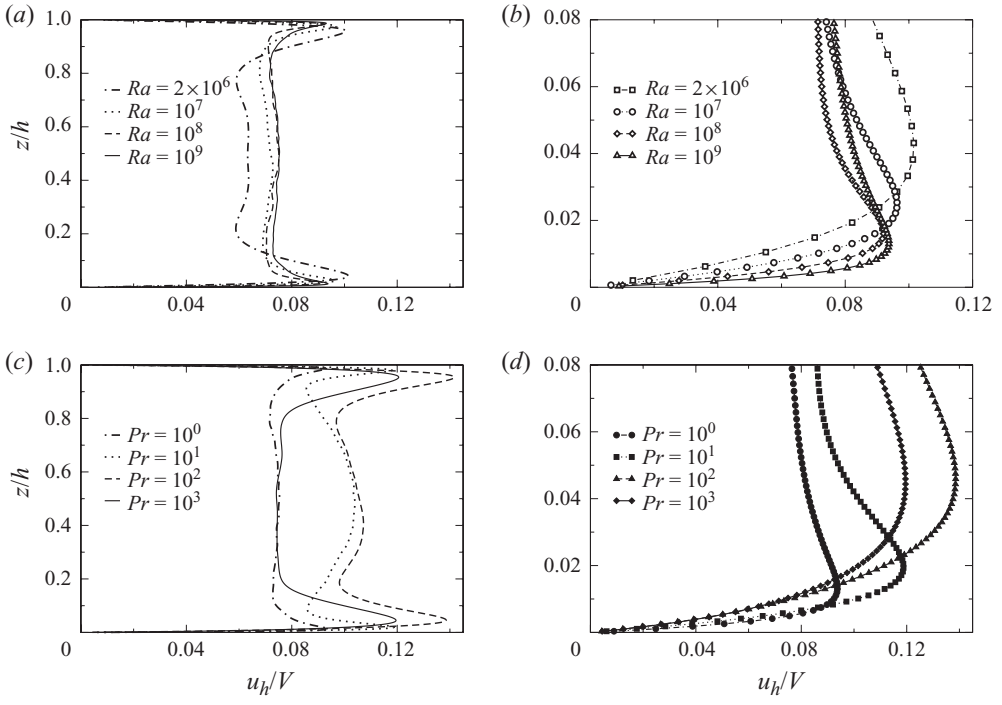

FIGURE 22. Global profiles of the horizontal-velocity r.m.s. (*a*, *b*) at $Pr = 1$ and increasing Ra; (*c*, *d*) at $Ra = 10^9$ and increasing Pr. (*b*, *d*) Enlargements of the lower wall regions with grid-point distribution.

saturation roughly starts at $Re \simeq 40$, when Re is calculated using the time-averaged peak vertical velocity. At lower Re, the scatter of δ_U around a saturation value (nearly 1/10 of the cell height) is mainly related to the presence of different mean flow structures found at different Ra and high Pr. One would expect that the viscous thickness, when it saturates, reaches half of the cell. A saturation at 1/10 the cell height, instead of 1/2, basically derives from the definition of δ_U. The presence of a large-scale circulation, even at very high Pr, implies at least two peaks in the global profiles of the horizontal-velocity r.m.s., and therefore a thickness smaller than 1/2. Consequently, the saturation of δ_U can also be interpreted as a saturation in the vertical size of the large-scale circulation.

If we consider the thermal boundary layer to be driven by the viscous one, its thickness should also saturate, as it actually does. The Pe independence of Pr at sufficiently high Pr (figure 21*b*) is consistent with the corresponding saturation of δ_T (and vice versa).

It thus seems that the saturation of δ_U, owing to a finite cell, induces a saturation on δ_T. This reflects the behaviour of the Péclet number, which turns out to be independent of Pr. Consequently, $Re \sim 1/Pr$. Thus, Re strongly decreases for increasing Pr, which implies a fast saturation of δ_U with increasing Pr, and a fast approach of all the flow to the infinite-Pr limit.

The saturation argument, however, does not fully explain two unexpected behaviours: the slight increase of the thermal-boundary-layer thickness with increasing Pr before the saturation (figure 24), and the independence of Nu of Pr at $Ra = 10^9$ and $Pr \simeq 1$ (far from saturation) (figure 16). In the first case, if we consider a

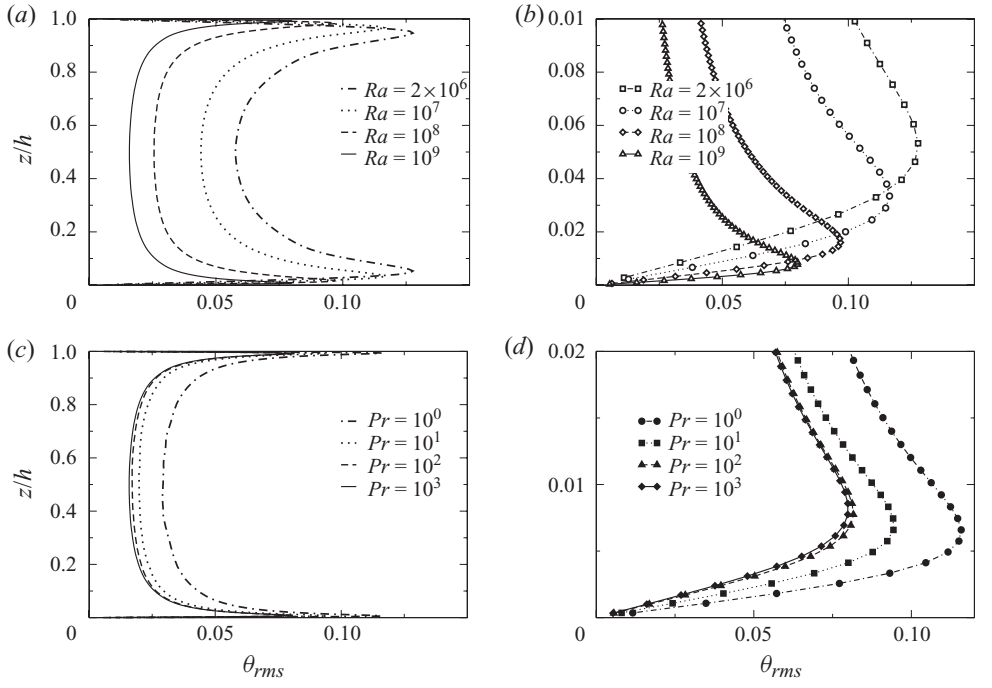

FIGURE 23. Global profiles of the temperature r.m.s. (*a*, *b*) at $Pr = 10^3$ and increasing Ra; (*c*, *d*) at $Ra = 10^9$ and increasing Pr. (*b*, *d*) Enlargements of the lower wall regions with grid-point distribution.

δ_T that is inversely related to the Péclet number, as predicted by the Prandtl–Blasius theory, δ_T should decrease as Pr increases, since Pe slightly increases with increasing Pr (figure 21*b*). This disagreement between δ_T and Pe could be due to uncertainties in their definition, since in both cases, the data trends show only a weak dependence on Pr. However, the Péclet number shows a slightly increasing trend with increasing Pr for sufficiently high Ra ($Ra \geqslant 10^8$), even when calculated by large-scale velocities different from that considered in figures 21(*b*) and 21(*d*). On the other hand, δ_T shows an increasing trend with Pr even when calculated as the depth corresponding to the intersection between diffusive and the convective heat-flux profiles ($-\langle \partial\Theta/\partial z\rangle_A = \langle u_z\Theta\rangle_A$), or as the depth corresponding to the intersection between the tangent to the temperature profile at the wall and the local tangent to the temperature profile in the bulk region. (Note that the last definition slightly differs from the usual one based on the tangent to the temperature profile at the wall and yields slightly different results.)

A possible explanation for the increasing behaviour of δ_T with Pr (for $Pr \gtrsim 1$) is that the thermal boundary layer is dragged up by the viscous boundary layer, as it becomes thicker than the thermal boundary. Indeed, figure 24(*b*) shows a strong discontinuity in the δ_T trend just when the viscous boundary layer becomes thicker than the thermal one. On the other hand, the idea that the viscous boundary layer, when thicker, governs the thermal one has been used widely (Kraichnan 1962; Shraiman & Siggia 1990; Grossmann & Lohse 2000). The above arguments on the saturation regime are essentially based on this hypothesis.

Instead, δ_T decreases with increasing Pr, that is, with increasing Péclet number (showing the expected inverse relation between δ_T and Pe) at low Pr before the

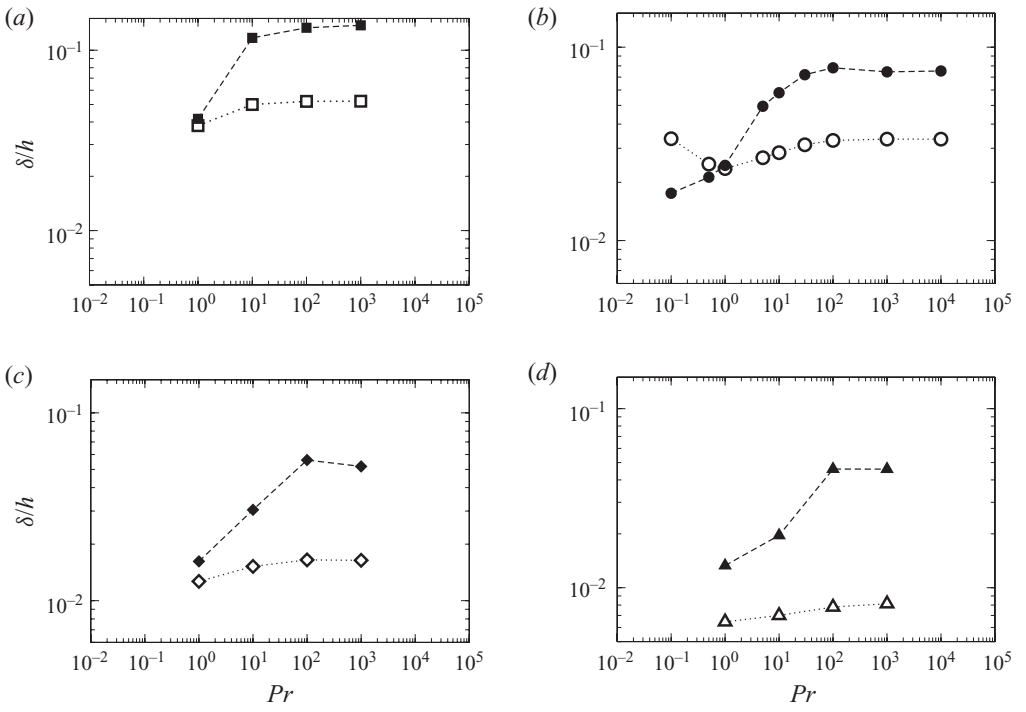

FIGURE 24. Boundary-layer thicknesses based on global r.m.s. profiles versus Pr. (a) $Ra = 2 \times 10^6$, (b) $Ra = 10^7$, (c) $Ra = 10^8$ and (d) $Ra = 10^9$. Bold open symbol–dotted line: thermal boundary layer; filled symbol–dashed line: viscous boundary layer. The difference between the top- and the bottom-plate values is generally much smaller than 1 %, both for thermal- and viscous-boundary-layer thicknesses. In few critical simulations, at lower Pr, the difference is smaller than 3 %. In any case, these differences are within the symbol size. This holds for all the figures concerning boundary-layer thicknesses.

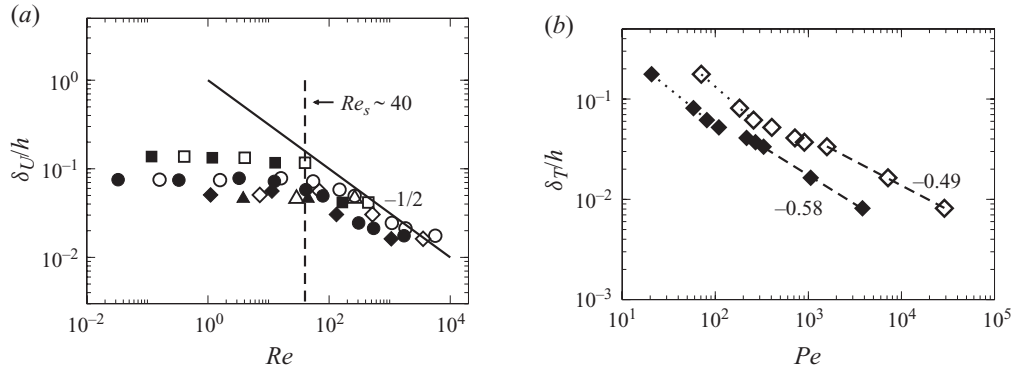

FIGURE 25. (a) Viscous-boundary-layer thickness with respect to the actual Reynolds number. Filled symbols: Re calculated using the maximum values of the horizontal-velocity r.m.s. profiles; open symbols: Re calculated using the time-averaged peak-vertical velocity. Squares: $Ra = 2 \times 10^6$; circles: $Ra = 10^7$; diamonds: $Ra = 10^8$; upright triangles: $Ra = 10^9$. (b) Thermal-boundary-layer thickness with respect to the actual Péclet number at $Pr = 10^3$. Filled symbols: Pe calculated using the maximum values of the horizontal-velocity r.m.s. profiles; open symbols: Pe calculated using the time-averaged peak-vertical velocity.

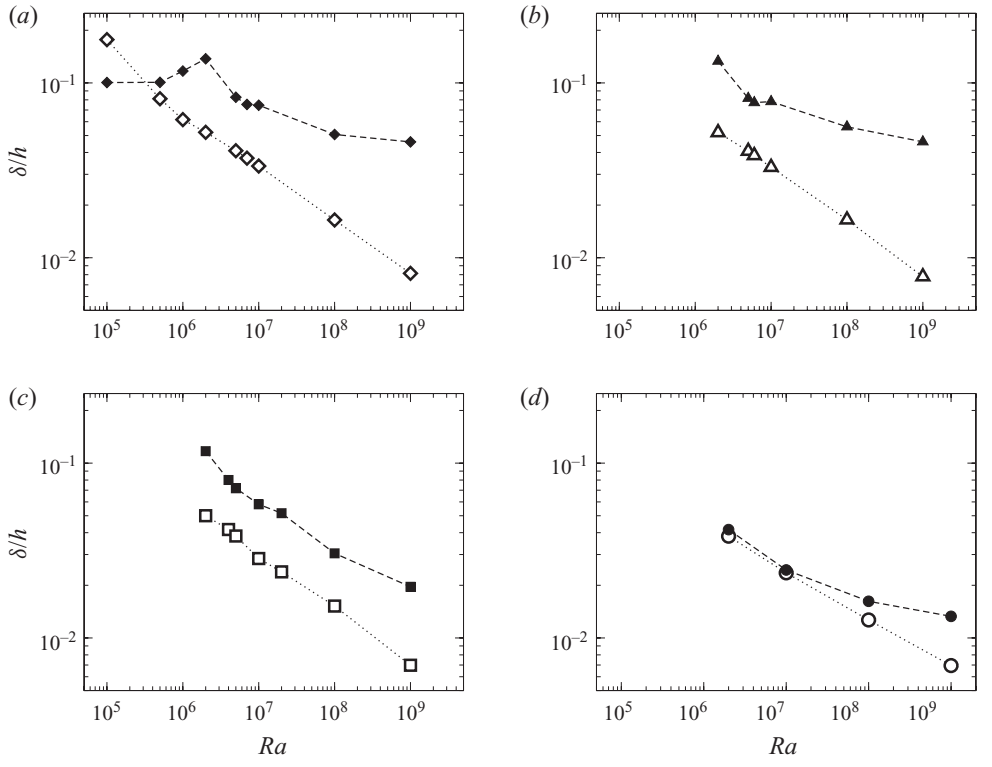

FIGURE 26. Boundary-layer thicknesses based on global r.m.s. profiles. (*a*) $Pr = 1000$, (*b*) $Pr = 100$, (*c*) $Pr = 10$ and (*d*) $Pr = 1$. Notation same as in figure 24.

change of hierarchy occurs between thermal and viscous boundary layers (figure 24*b*) at higher Pr, prior to the saturation because of the cell height (Breuer *et al.* 2004).

Overall, it thus seems that there are two opposite effects acting on the thermal-boundary-layer thickness: the Péclet-number influence, which tends to bring it down, and the viscous-boundary-layer influence, which tends to lift it up. The balance between the two effects determines the boundary-layer thickness.

In the range of Ra simulated here, generally the viscous-boundary-layer effect is slightly stronger than the Pe effect when δ_T is calculated using the peak values of the r.m.s. temperature profile. When δ_T is calculated as the intersection between the tangent to the temperature profile at the wall and the straight line of the central-temperature value across the cell height, the two effects mostly balance each other and δ_T becomes almost constant with Pr, even far from saturation. As a consequence, the Nusselt number, because of the exact relation (2.4), reflects the same trend, resulting in its being independent of Pr (even at $Ra = 10^9$ and $Pr \simeq 1$).

For completeness, we now show the trends of the boundary-layer thicknesses with respect to the Rayleigh number. Figure 26 shows the viscous- and thermal-boundary-layer thicknesses as a function of Ra. The high scatter of δ_U for various Ra and high Pr (figures 26*a* and 26*b*) is due to the different mean flow structures. The viscous- and thermal-boundary-layer thicknesses are generally expected to follow the same trend in the Prandtl–Blasius theory. However, because of the δ_U saturation with respect to Re (figure 25*a*), the trend of δ_U with respect to Ra deviates from that of δ_T at high Pr. In agreement with previous results (Belmonte, Tilgner & Libchaber 1993;

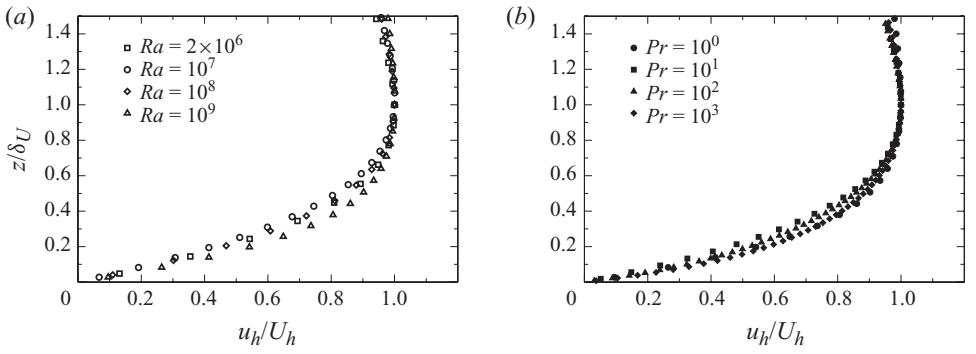

FIGURE 27. Global profiles of the horizontal-velocity r.m.s. (*a*) at $Pr = 1$ and increasing Ra; (*b*) at $Ra = 10^9$ and increasing Pr. The profiles are normalized with respect to their maximum value and the corresponding height.

Verzicco & Camussi 2003), we have also found a difference between the trends of δ_U and δ_T at lower Pr (figures 26*d* and 30*a*). This deviation at $Pr = 1$ seems to be a temporary effect, due to a difference in the mean flow structures, tending to disappear at $Ra > 10^{10}$ (Verzicco & Camussi 2003).

The exponent of a power-law fitting δ_T versus Ra is approximately 0.3, if we consider the data at fixed Pr for $Ra \geqslant 10^7$. Figure 25(*b*) shows the behaviour of thermal-boundary-layer thickness with respect to Pe at fixed $Pr = 10^3$. The two data trends are evaluated using different typical velocities for the calculation of Pe. When the peak vertical velocity is considered, the trend seems to be consistent with the Prandtl–Blasius theory. However, it would be more reasonable to consider an horizontal velocity as characteristic of the boundary layers at the plates, but, in this latter case, no consistency in the results has been found.

While a few qualitative consistencies of the boundary-layer thicknesses exist with the Prandtl–Blasius theory, we find no similarly in velocity profiles. Indeed, the profiles do not show a constant shape close to the plates, either in terms of Ra (figure 27*a*), or in terms of Pr (figure 27*b*). In the first case, no similarity has been found even at $Pr = 1$, when the mean flows show similar large-scale structures and the local profile shapes (see later) are similar to each other (figure 28*a*). This is in contrast to experimental results shown in Lam *et al.* (2002), concerning a cylindrical cell of aspect ratio 1.

6.2. *Local and global thicknesses*

An open question is how the boundary-layer thicknesses based on the global profile (averaged in time and over the horizontal sections) are related to those based on local profiles (averaged only in time) (Ahlers *et al.* 2009). The boundary-layer thickness is actually a local feature of the mean flow, even if, from the theoretical point of view, the global profiles and the corresponding thicknesses are of main interest, because they are strongly characterized by symmetry and show exact analytical relationships that can be used in the models (see, for example, Grossmann & Lohse 2000). Moreover, in the presence of different mean flow structures and flow inversions inside the boundary layers, it is not easy to compare the local profiles and evaluate local boundary-layer thicknesses. For this reason, area-averaged profiles, characterized by a single value, are preferred in data analysis. The issue is to understand if, and how, the global profiles can represent local features.

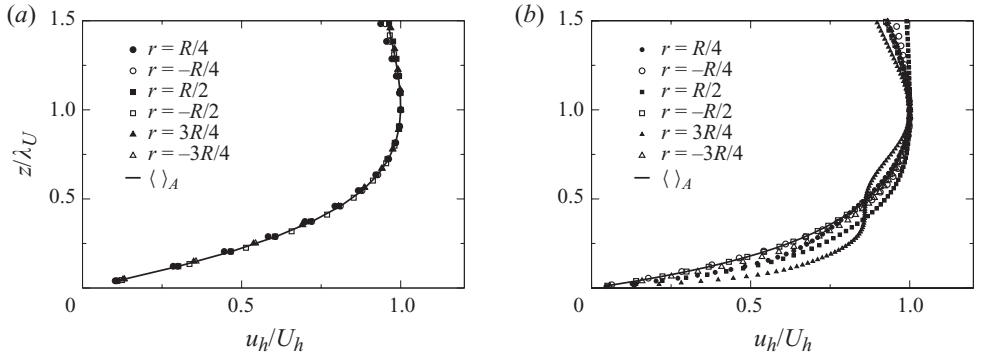

FIGURE 28. Local profiles of horizontal-velocity r.m.s. compared to the global one. (*a*) $Ra = 10^8$ and $Pr = 1$; (*b*) $Ra = 10^8$ and $Pr = 10^3$. The profiles are normalized with respect to their maximum value and the corresponding height. The local profile (time-averaged only) belongs to the vertical section relative to the maximum circulation development at various radial positions, in comparison to the area-averaged profile (solid line). Here r and R are respectively the radial coordinate (ranging between 0 and R) and the radius of the cylindrical domain.

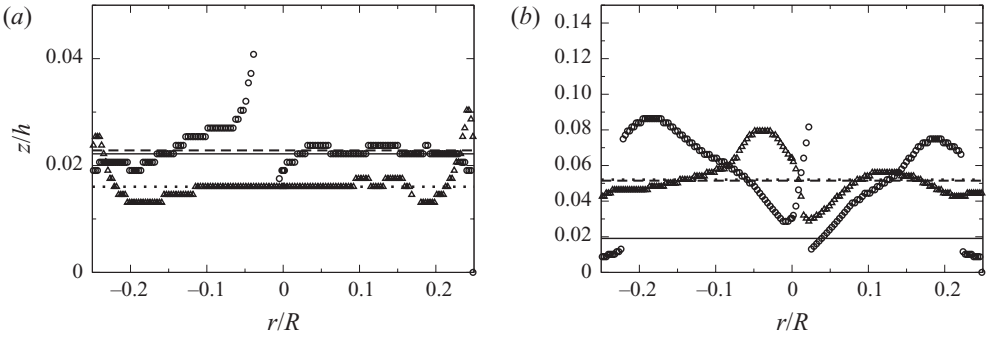

FIGURE 29. Viscous-boundary-layer thickness distribution along the bottom plate in a vertical section corresponding to the maximum development of the mean flow circulation. Circles: λ_U^{max}; upright triangles: λ_U^{rms}. Dashed line: $\langle \lambda_U^{max} \rangle_r$; solid line: δ_U^{max}; dotted line: δ_U^{rms}. (*a*) $Ra = 10^8$ and $Pr = 1$; (*b*) $Ra = 10^8$ and $Pr = 10^3$. The strong discontinuity of the local thickness λ_U^{max} at the central axis and close to the sidewall is due to the flow structure characterized by a descending circulation at the central axis and an ascending one close to the sidewall in (*a*) and vice versa in (*b*).

When the flow shows opposite circulations, the area-averaged velocity profile tends to disappear. As a consequence, in order to define a viscous-boundary-layer thickness based on a global velocity profile and valid for all the simulations, the r.m.s. of the area-averaged horizontal velocity has to be considered. Comparing the local and global profiles of the r.m.s. of the horizontal velocity, we found a good similarity (figure 28*a*) when the mean flow consists of two opposite toroidal structures ($Pr < 100$). Instead, a poorer correspondence has been found for flows at $Pr \geqslant 100$, characterized by lower Reynolds numbers and multi-jet structures, and therefore having no well-developed viscous boundary layers (figure 28*b*).

We analyse the local viscous-boundary-layer thickness λ_U (figure 29), calculated using the maximum of the local profiles of the horizontal velocity (λ_U^{max}) as well as the horizontal-velocity r.m.s. (λ_U^{rms}) and find the following result: for $Pr = 1$, these thicknesses, averaged along the section of maximum circulation development

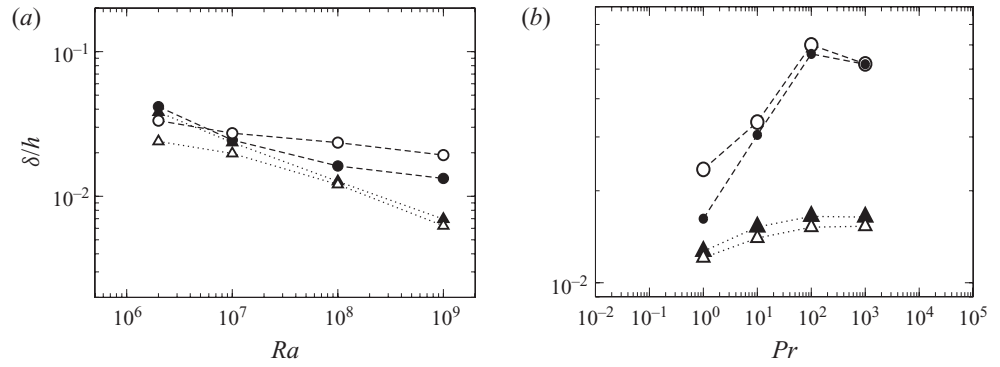

FIGURE 30. Global-boundary-layer thicknesses (filled symbols) compared to the local ones (open symbols). Filled circles: δ_{Urms}; open circles: $\langle\lambda_{Umax}\rangle_r$; filled upright triangles: δ_{Trms}; open upright triangles: $\langle\lambda_{Trms}\rangle_r$. (*a*) Fixed $Pr = 1$; (*b*) fixed $Ra = 10^8$.

(excluding narrow regions close to the sidewall and the central axis), basically are the same as the corresponding global thicknesses: $\langle\lambda_U^{max}\rangle_r \simeq \delta_U^{max}$ and $\langle\lambda_U^{rms}\rangle_r \simeq \delta_U^{rms}$ (figure 29*a*). For higher Pr, however, the area-averaged profiles of the horizontal velocity almost vanish and δ_U^{max} loses its meaning, while a satisfactory correspondence between $\langle\lambda_U^{max}\rangle_r$ and δ_U^{rms} is found (figure 29*b*). In particular, in the simulations at $Pr = 10^3$, we found that δ_U^{rms} differs from $\langle\lambda_U^{max}\rangle_r$ by less than 3 %. Thus, for higher Pr, the global thickness δ_U^{rms} adequately represents the local thickness λ_U^{max} based on the maximum of the horizontal-velocity profiles (figure 30*b*). This is not surprising since the velocity fluctuations strongly decrease as Pr increases. At $Pr \sim 1$, δ_U^{rms} generally underestimates λ_U^{max} (discrepancies around 8 %), but the two thicknesses follow the same trend at sufficiently high Ra (figure 30*a*).

Similar analysis has been performed for the thermal-boundary-layer thicknesses. In particular, we have compared the local and global thicknesses based on the temperature–r.m.s. profiles. In this case, a satisfactory agreement between the trends of the two thicknesses have been generally found (figure 30), since the Péclet numbers are high enough ($Pe > 10^3$) to obtain sufficiently developed thermal boundary layers. Indeed, we generally found λ_T^{rms} to be quite uniform along the plate, except for narrow regions close to the sidewall. The higher discrepancies are at $Pr = 1$ and lower Ra, corresponding to smaller Pe (figure 30*a*).

As a conclusion, in the range of Ra and Pr explored in this study, the trends of the local boundary-layer thicknesses are essentially the same as those of the global ones. Given the higher reliability in a practical calculation, it thus stands to reason that we have considered the thicknesses based on the global profiles.

7. Conclusions

In this study, we have investigated the main features of the thermal convection at moderate Ra over a range of Prandtl numbers with emphasis on high values. By direct numerical simulations of the Boussinesq equations in a cylindrical domain of aspect ratio 1/2, we have replicated the set-up of several experimental and past numerical works. In particular, by simulating the convective flow at quite high Pr ($Pr \sim O(10^3)$), we have explored an Ra–Pr range, which, until now, was approachable only through laboratory experiments or simplified numerical models.

The high-Pr flows are generally characterized by high Péclet numbers and low Reynolds numbers. This implies that the temperature field is mainly governed by

advective dynamics, and the velocity field is mainly governed by diffusive phenomena. The combination of these opposite features generates the convection dynamics at high Pr. The combination of these different dynamics is reflected in the typical large-scale velocities and in the corresponding typical time scales. The free-fall velocity $U = \sqrt{g\alpha\Delta T h}$, arising from the balance between the inertial term and the buoyancy term of the momentum equation, was inadequate for representing the typical velocities at high Pr, which are much smaller. The usual alternative velocities, characteristic of the diffusive dynamics, obtained by balancing the buoyancy and viscous terms of the momentum equation, or by comparing the advective and diffusive terms of the temperature equation, were also inadequate (this time because of their dependence on Ra). By scaling the results from several simulations, we found that the suitable characteristic velocity of the large-scale convective dynamics is $V = U/\sqrt{Pr}$. This velocity represents a synthesis between the diffusive characteristic velocities and the free-fall velocity, maintaining the dependence of diffusive velocities on Pr, and the dependence of the free-fall velocity on Ra.

Using this new characteristic velocity, we derived the suitable non-dimensional form of the Boussinesq equations for high-Pr flows, and a rough estimate of Re and Pe as functions of Ra and Pr, obtaining $Re = \sqrt{Ra}/Pr$, and, consequently, $Pe = \sqrt{Ra}$ independent of Pr. From the comparison of these estimates with the actual Re and Pe trends, it was clear that they represent a good first-order approximation of the Re and Pe behaviour, but a single scaling was insufficient to match all the data in the range of simulated Ra and Pr: a power-law relation did not always appear to be appropriate to fit the data exactly, and seem to require logarithmic corrections to the main power-law trends. Further uncertainties derive from the velocity that one defines as typical of large-scale dynamics. Nevertheless, the Re and Pe estimates (mentioned above) are able to capture the main trends, especially with respect to Pr, when Pr is sufficiently high and a saturation regime is approached.

The saturation regime is a main feature of the confined flows with increasing Pr. It is due to the fact that the viscous boundary layer, induced by the large-scale recirculations, cannot indefinitely grow as Re decreases (Pr increases), at least because the cell has a finite size. We found that, in a cell of aspect ratio 1/2, the saturation of the viscous-boundary-layer thickness starts approximately at $Re_s \simeq 40$ (with Re calculated using the time-averaged peak vertical velocity). The saturation of the viscous boundary layer induces a saturation in the thermal boundary layer thickness (which is apparently influenced by the viscous boundary layer when the latter is thicker than the former). The independence of Péclet number of Pr reflects the saturation of the thermal boundary layer. Consequently, $Re \sim 1/Pr$, implying a fast saturation of the viscous boundary layer with increasing Pr.

The Nusselt number is strongly related to the thermal boundary layer, since the former is determined by the temperature drop which occurs close to the horizontal plates, but it is not strongly affected by flow structures. Our simulation data show Nu independent of Pr, for $Pr \gtrsim 1$. This result, even characterizing the highest Ra simulated ($Ra = 10^9$), can be justified by saturation arguments only when the saturation occurs – that is, for sufficiently high Pr ($Pr \gtrsim 100$). At lower Pr, the independence of Nu of Pr is due to the balance between two opposite effects acting on the thermal boundary: the Péclet number influence, which tends to lower it (since Pe slightly increases with increasing Pr before the saturation is reached), and the viscous-boundary-layer influence, which tends to enhance it (since the viscous boundary layer grows with increasing Pr). In general, the thermal dissipation is turbulent-like even when the viscous dissipation is laminar-like.

By using previous results at lower Pr and comparing them to our data, we confirm the presence of a lower Pr regime, where approximately $Re \sim Pr^{-0.7}$, and a saturation regime at high Pr, where $Re \sim Pr^{-1}$. The beginning of the saturation regime depends on a critical Reynolds number (Re_s), beyond which the viscous boundary layer, or, conversely, the large-scale circulation, saturates to a constant size: roughly 2/10 of the cell depth is occupied by the boundary layers and 8/10 by large-scale circulations, when the viscous-boundary-layer thickness is based on the r.m.s. profile of the horizontal velocity. However, the approach to saturation seems to be smooth, and the saturation regime seems to affect (or to be affected by) the preceding Pr interval, until the hierarchy between thermal- and viscous-boundary-layer changes.

The presence of the viscous boundary layer, however, does not seem to be a necessary condition for the observation of a saturation regime. Indeed, a qualitatively similar Re–Pr scaling was also obtained in simulations carried out under a free-slip boundary condition (Breuer *et al.* 2004). In this case, it is possible to hypothesize the saturation of the large-scale circulations instead of the viscous boundary layer, but the other arguments on the interaction between viscous and thermal boundary layers do not seem to be valid. However, even without viscous boundary layers, the large-scale motion generates strong velocity gradients close to the walls, which can substitute the viscous-boundary-layer arguments in the explanation of the thermal-boundary-layer behaviour at high-Pr regimes. In spite of its unclear role, the viscous boundary layer is the base of many models for scaling predictions of thermal convection. The usual assumption is to consider the Prandtl–Blasius theory (Grossmann & Lohse 2000), which regards the temperature field as a passive scalar and implies similarity solutions. In the Ra–Pr range considered here, inside the boundary layers we found no similarities with respect to Ra and Pr, either in velocity profiles or in temperature profiles. It should, however, be mentioned that in the present study, the boundary-layer thicknesses have been estimated from the r.m.s. peak positions, while, in Grossmann & Lohse (2000), they are essentially defined using the slopes at the wall of the mean profiles. It is not clear if the different definitions can cause any disagreement. This point deserves further investigation.

The large-scale simulations in this paper were possible due to the support and computer facilities of the Consorzio interuniversitario per le Applicazioni di Supercalcolo Per Università e Ricerca (CASPUR). We gratefully acknowledge Drs F. Massaioli and G. Amati for their continuous technical support. The work formed part of the PhD thesis of G.S. at the University of Trieste.

REFERENCES

Ahlers, G., Grossmann, S. & Lohse, D. 2009 Large-scale dynamics in turbulent Rayleigh–Bénard convection. *Rev. Mod. Phys.* **81**, 503–537.

Ahlers, G. & Xu, X. 2001 Prandtl-number dependence of heat transport in turbulent Rayleigh–Bénard convection. *Phys. Rev. Lett.* **86**, 3320–3323.

Ashkenazi, S. & Steinberg, V. 1999 High Rayleigh number turbulent convection in a gas near the gas–liquid critical point. *Phys. Rev. Lett.* **83**, 3641–3644.

Batchelor, G. K. 1959 Small scale variation of convected quantities like temperature in turbulent fluid. *J. Fluid Mech.* **5**, 113–133.

Belmonte, A., Tilgner, A. & Libchaber, A. 1993 Boundary layer length scales in thermal turbulence. *Phys. Rev. Lett.* **70**, 4067.

Bénard, H. 1900 Les tourbillons cellulaires dans une nappe liquide. *Revue Gen. Sci. Pures Appl.* **11**, 1261–1271.

Bodenschatz, E., Pesch, W. & Ahlers, G. 2000 Recent developments in Rayleigh–Bénard convection. *Annu. Rev. Fluid Mech.* **32**, 709–778.

Boronska, K. & Tuckerman, L. S. 2006 Standing and travelling waves in cylindrical Rayleigh–Bénard convection. *J. Fluid Mech.* **559**, 279–298.

Boronska, K. & Tuckerman, L. S. 2010 Extreme multiplicity in cylindrical Rayleigh–Bénard convection: I. time-dependence and oscillations. *Phys. Rev.* E **81**, 036321.

Breuer, M., Wessling, S., Schmalzl, J. & Hansen, U. 2004 Effect of inertia in Rayleigh–Bénard convection. *Phys. Rev.* E **69**, 026302.

Brown, E. & Ahlers, G. 2009 The origin of oscillations of the large-scale circulation of turbulent Rayleigh–Bénard convection. *J. Fluid Mech.* **638**, 383–400.

Brown, E., Funfschilling, D. & Ahlers, G. 2007 Anomalous Reynolds-number scaling in turbulent Rayleigh–Bénard convection. *J. Stat. Mech.* P10005.

Calzavarini, E., Lohse, D., Toschi, F. & Tripiccione, R. 2005 Rayleigh and Prandtl number scaling in the bulk of Rayleigh–Bénard turbulence. *Phys. Fluids* **17**, 055107.

Castaing, B., Guranatne, G., Heslot, F., Kadanoff, L., Libchaber, A. & Thomae, S. 1989 Scaling of hard thermal turbulence in Rayleigh–Bénard convection. *J. Fluid Mech.* **204**, 1–30.

Chandrasekar, S. 1961 *Hydrodynamic and Hydromagnetic Stability*. Oxford Univ. Press.

Charlson, G. S. & Sani, R. L. 1970 Thermoconvective instability in a bounded cylindrical fluid layer. *Intl J. Heat Mass Transfer* **13**, 1479–1496.

Chavanne, X., Chilla, F., Castaing, B. & Hebral, B. 2001 Turbulent Rayleigh–Bénard convection in gaseous and liquid He. *Phys. Fluids* **13**, 1300–1320.

Clever, R. & Busse, F. 1974 Transition to time-dependent convection. *J. Fluid Mech.* **65**, 625–645.

Croquette, V., Le Gal, P. & Pocheau, A. 1986 Spatial features of the transition to chaos in an extended system. *Phys. Scripta* T **13**, 135.

Daya, Z. A. & Ecke, R. E. 2001 Does turbulent convection feel the shape of the container? *Phys. Rev. Lett.* **87** (18), 184501.

Donzis, D. A., Sreenivasan, K. R. & Yeung, P. K. 2010 The Batchelor spectrum for mixing of passive scalars in isotropic turbulence. *Flow, Turb. Combust.* (in press).

Emran, M. S. & Schumacher, J. 2008 Fine-scale statistics of temperature and its derivatives in convective turbulence. *J. Fluid Mech.* **611**, 13–34.

Grossmann, S. & Lohse, D. 2000 Scaling in thermal convection: a unifying theory. *J. Fluid Mech.* **407**, 27–56.

Grossmann, S. & Lohse, D. 2001 Thermal convection for large Prandtl numbers. *Phys. Rev. Lett.* **86**, 3316–3319.

Hardin, G. R. & Sani, R. L. 1993 Weakly non-linear solutions. *Intl J. Numer. Meth. Fluids* **17**, 755.

Heslot, F., Castaing, B. & Libchaber, A. 1987 Transitions to turbulence in helium gas. *Phys. Rev.* A **36**, 5870–5873.

Hof, B., Lucas, G. J. & Mullin, T. 1999 Flow state multiplicity in convection. *Phys. Fluids* **11**, 2815–2817.

Kerr, R. M. & Herring, J. R. 2000 Prandtl number dependence of Nusselt number in direct numerical simulations. *J. Fluid Mech.* **419**, 325–344.

Kolmogorov, A. N. 1941 The local structure of turbulence in incompressible viscous fluid for a very large Reynolds numbers. *Proc. R. Soc. Lond.* A **434**, 9–13.

Kraichnan, R. H. 1962 Turbulent thermal convection at arbitrary Prandtl number. *Phys. Fluids* **5**, 1374–1389.

Krishnamurti, R. & Howard, L. N. 1981 Large-scale flow generation in turbulent convection. *Proc. Natl Acad. Sci.* **78** (4), 1981–1985.

Lam, S., Shang, X., Zhou, S. & Xia, K. 2002 Prandtl number dependence of the viscous boundary layer and the Reynolds numbers in Rayleigh–Bénard convection. *Phys. Rev. Lett.* E **65**, 066306.

Niemela, J. J., Skrbek, L., Sreenivasan, K. R. & Donnelly, R. J. 2000 Turbulent convection at very high Rayleigh numbers. *Nature* **404**, 837–840.

Niemela, J. J., Skrbek, L., Sreenivasan, K. R. & Donnelly, R. J. 2001 The wind in confined thermal convection. *J. Fluid Mech.* **449**, 169–178.

Niemela, J. J. & Sreenivasan, K. R. 2003 Confined turbulent convection. *J. Fluid Mech.* **481**, 355–384.

Oresta, P., Stringano, G. & Verzicco, R. 2007 Transitional regimes and rotation effects in Rayleigh–Bénard convection in a slender cylindrical cell. *Eur. J. Mech.* B/*Fluids* **26** (1), 1–14.

Peltier, W. R. 1989 *Mantle Convection: Plate Tectonics and Global Dynamics*. Gordon and Breach.

Prandtl, L. 1952 *Essentials of Fluid Mechanics*, Chapter V. Hafner.

Rayleigh, Lord 1916 On convective currents in horizontal layer of fluid when the higher temperature is on the under side. *Phil. Mag.* **32**, 529–546.

Roche, P. E., Castaing, B., Chabaud, B. & Hébral, B. 2002 Prandtl and Rayleigh numbers dependencies in Rayleigh–Bénard convection. *Europhys. Lett.* **58**, 693–698.

Rudiger, S. & Feudel, F. 2000 Patter formation in Rayleigh–Bénard convection in a cylindrical container. *Phys. Rev.* E **62**, 4927–4931.

Schmalzl, J., Breuer, M. & Hansen, U. 2002 The influence of the Prandtl number on the style of vigorous thermal convection. *Goephys. Astrophys. Fluid Dyn.* **96**, 381–403.

Schumacher, J., Sreenivasan, K. R. & Yeung, P. K. 2005 Very fine structures in scalar mixing. *J. Fluid Mech.* **531**, 113–122.

Shishkina, O. & Thess, A. 2009 Mean temperature profiles in turbulent Rayleigh–Bénard convection of water. *J. Fluid Mech.* **633**, 449–460.

Shishkina, O. & Wagner, C. 2008 Analysis of sheet-like thermal plumes in turbulent Rayleigh–Bénard convection. *J. Fluid Mech.* **599**, 383–404.

Shraiman, B. I. & Siggia, E. D. 1990 Heat transport in high-Rayleigh number convection. *Phys. Rev.* A **42**, 3650–3653.

Silano, G. 2009 Numerical simulations of thermal convection at high Prandtl numbers. PhD thesis, University of Trieste, http://hdl.handle.net/10077/3211.

Spalart, P. R. & Moser, R. D. 1991 Spectral methods for the Navier-Stokes equations with one infinite and two periodic directions. *J. Comput. Phys.* **96**, 297–324.

Stevens, R. J. A. M., Verzicco, R. & Lohse, D. 2010 Radial boundary layer structure and Nusselt number in Rayleigh–Bénard convection. *J. Fluid Mech.* **643**, 495–507.

Threlfall, D. C. 1975 Free convection in low-temperature gaseous helium. *J. Fluid Mech.* **67**, 17–28.

Tritton, D. J. 1988 *Physical Fluid Dynamics*, 2nd edn. Clarendon Press.

Umemura, A. & Busse, F. H. 1989 Axisymmetric convection at large Rayleigh number and infinite Prandtl number. *J. Fluid Mech.* **208**, 459–478.

Verzicco, R. 2003 Turbulent thermal convection in a closed domain: viscous boundary layer and mean flow effects. *Eur. Phys. J.* B **35**, 133–141.

Verzicco, R. & Camussi, R. 1997 Transitional regimes of low-Prandtl thermal convection in a cylindrical cell. *Phys. Fluids* **9**, 1287–1295.

Verzicco, R. & Camussi, R. 1999 Prandtl number effects in convective turbulence. *J. Fluid Mech.* **383**, 55–73.

Verzicco, R. & Camussi, R. 2003 Numerical experiments on strongly turbulent thermal convection in a slender cylindrical cell. *J. Fluid Mech.* **477**, 19–49.

Verzicco, R. & Orlandi, P. 1996 A finite-difference scheme for three-dimensional incompressible flows in cylindrical coordinates. *J. Comput. Phys.* **123**, 402–414.

Xia, K., Liam, S. & Zhou, S. 2002 Heat-flux measurement in high-Prantdl-number turbulent Rayleigh–Bénard convection. *Phys. Rev. Lett.* **88**, 064501.

Zhou, Q. & Xia, K. Q. 2008 Comparative experimental study of local mixing of active and passive scalar in turbulent thermal convection. *Phys. Rev.* E **77**, 056312.